The Discontinuous Galerkin Method Applied to Problems in Electromagnetism

by

Dale Connor

A thesis
presented to the University of Waterloo
in fulfillment of the
thesis requirement for the degree of
Master of Mathematics
in
Applied Mathematics

Waterloo, Ontario, Canada, 2012

© Dale Connor 2012

I hereby declare that I am the sole author of this thesis. This is a true copy of the thesis, including any required final revisions, as accepted by my examiners.

I understand that my thesis may be made electronically available to the public.

Abstract

The discontinuous Galerkin method (DGM) is applied to a number of problems in computational electromagnetics. This is achieved by obtaining numerical solutions to Maxwell's equations using the DGM. The aim of these simulations is to highlight the strengths of the method while showing its resilience in handling problems other schemes may not be able to accurately model.

Although no method will ever be the best choice for every problem in electromagnetics, the discontinuous Galerkin method is able to accurately approximate any problem, although the computational costs can make the scheme impractical for some. Like other time domain schemes, the DGM becomes inefficient on large domains where the solution contains small wavelengths.

We demonstrate that all of the different types of boundary conditions in electromagnetic wave propagation can be implemented into the DGM. Reflection and transmission boundaries fit easily into the framework, whereas perfect absorption requires a more advanced technique known as the perfectly matched layer. We begin by simulating mirrors with several different geometries, and analyze how the DGM method performs, and how it offers a more complete evaluation of the behavior in this problem than some other methods.

Since Maxwell's equations describe the macroscopic features of electromagnetics, our simulations are able to capture the wave features of electromagnetics, such as interference and diffraction. We demonstrate this by accurately modelling Young's double slit experiment, a classic experiment which features well understood interference and diffraction phenomena.

We also extend the basic electromagnetic wave propagation simulations to include situations where the waves travel into new media. The formulation of the DGM for Maxwell's equations allows the numerical solutions to accurately resolve the features at the interface of two media as predicted by the Fresnel coefficients. This allows the DGM to model lenses and other sources of refraction.

We predict that the DGM will become an increasingly valuable method for computational electromagnetics because of its wide range of applicability as well as the lack of undesirable features in the numerical solutions. Furthermore, the only limiting factor for applying DGM, its computational cost, will become less influential as computing power continues to increase, allowing us to apply the DGM to an increasing set of applications.

Acknowledgements

I would like to thank my advisor Lilia Krivodonova for her advice, patience, and guidance since I began working with her years ago. I am grateful for all that you have taught me and all the opportunities you led me too. I thank you for your efforts to get me involved in mathematics, and for the wealth of information you were able to pass on to me. I cannot imagine how I would have completed this without your insight and encouragement.

I would also like to thank Daniel Hailu, Safieddin Safavi-Naeini, and the rest of their group in engineering for providing me with motivation to press on, as well as sharing with me their experience in the field. Their input had an important influence on this project and I am grateful for the knowledge I learned from them.

Thank you to the staff in the Department of Applied Mathematics for all of their assistance during my time here. I thank Helen Warren for everything she has done for me, from helping me with every last detail I was not sure about to keeping myself, and every other grad student, on track. Although I am not always certain how she does it all, I am very grateful she does.

I would also like to thank Marek Stastna and Hans De Sterck for taking the time to read my thesis and provide me with helpful comments and corrections.

Lastly, thank you Mom and Dad for your love and support. Thank you keeping my feet on the ground when it felt like there was too much to handle.

Table of Contents

List of Tables **vii**

List of Figures **viii**

1 Introduction **1**

1.1 Applications of Electromagnetic Simulations 1

1.2 Numerical Methods for Electromagnetic Problems 3

1.3 Maxwell's Equations and the TM mode 8

2 DGM Concept for Electromagnetics **12**

2.1 Why DGM? 12

2.2 Boundaries and Surfaces 14

2.3 Diffraction 16

2.4 The Practical Range of DG 19

3 Discontinuous Galerkin Formulation for Maxwell's Equations **22**

3.1 Meshing 22

3.2 Formulation 23

3.3 Riemann Problem 31

3.4 Numerical Boundary Conditions 34

3.5 Initial Conditions and Source Terms 37

3.6 Sensors and Data 39

4 Numerical Examples **41**

4.1 Coffee Cup Caustic 41

4.2 Young's Double Slit Experiment 52

4.3 Less Ideal Geometries - Parabolic and Hyperbolic Mirrors 59

4.4 Refraction 63

4.5 Total Internal Reflection 68

4.6 Cylindrical Lens 69

5 Conclusion and Future Work **75**

References **77**

List of Tables

4.1 Maximum value of time averaged intensity obtained in at the focal point. . 46
4.2 Location of the focal point from the circular mirror. 46
4.3 Relative time taken for simulations compared to $h = h_2$, $p = 2$ case. 48

List of Figures

2.1 A single wavelength of a sine wave initiated in air interacting with a glass wedge, showing various types of reflections 15

2.2 Plane waves originating at the left boundary strike an aperture as depicted in left figure. Diffraction occurs causing the plane wave to seemingly wrap around the edges of the aperture. 18

2.3 A Gaussian beam propagating in both directions from the the Gaussian source at x=0 in the middle of the domain. 19

3.1 Sketch of the three wave speeds from TM Maxwell's equations. Three discontinuities are present at the interface described by the eigenvalues λ_1, λ_2, and λ_3 which define their propagation speeds. 33

4.1 The coffee cup caustic simulated using POV-Ray, a 3D geometrical optics software package 42

4.2 A demonstration of paraxial rays (which are blue upon reflection) which intersect at the expected focal point, and non-paraxial rays (which are red upon reflection) which cause spherical aberrations. 43

4.3 A 9193 element mesh used to simulate plane waves striking a circular mirror 44

4.4 A large cell (in black) is refined to make four smaller cells (in red). The smaller cells better adapt to the physical boundary so the numerical domain converges to the physical one. 46

4.5 Time averaged intensity from a circular mirror obtained using different combinations of *hp*-refinement. Top row is the unrefined mesh (figure 4.3), each row below is one further level of h-refinement. Leftmost column are simulations with $p = 1$, middle column uses $p = 2$ and on the right, $p = 3$. 47

4.6 The time averaged intensity from the simulation of a high frequency, planar source. 49

4.7 The time averaged intensity from the simulation ($h = h_2$, $p = 2$) of a single pulse propagating through the domain. 51

4.8 The electric field from the planar pulse at 4 different time steps increasing in time from left to right. 52

4.9 Three dimensional plots of the data in figure 4.8. 52

4.10 Mesh for simulating Young's double slit experiment 55

4.11 On the left, the electric field at one instant in time. On the right, the intensity distribution through the slits at that same instant. 56

4.12 Time averaged intensity from modelling Young's experiment with a logarithmic colour scale. On the right, filled isolines of the solution. The left image has been rotated in space. 57

4.13 Intensity data from three instances in time (top), and the maximum of all sampled moments in time showing the amplitude of the oscillations in intensity along the line $x = 2.4$. 58

4.14 Simulation data compared to linear Fraunhofer solution. 58

4.15 Simulation data compared to Fraunhofer solution. 59

4.16 Mesh used to simulate the parabolic reflector 60

4.17 Electric field of a plane wave hitting a parabolic reflector at five different moments in time, progressing in time moving left to right. 61

4.18 Time averaged intensity of the simulation of a parabolic reflector, on the right a zoom in of the focal region showing the high level of accuracy . . . 62

4.19 The mesh for simulations involving the parabolic-hyperbolic pair of reflectors. 63

4.20 Images of the electric field at six different points in time as the pulse propagates through the domain. 64

4.21 Time averaged intensity of the effects of a planar wave in a classical Cassegrain reflector. 65

4.22 Snells Law for two media with indices of refraction of n_1 and n_2 65

4.23 Mesh for modelling refraction between two media. The verticle line in the middle of the domain denotes the boundary between the different media. . 66

4.24 Refraction with angles. Left: a ray path for the solution with theoretical angles of incidence and reflection. Right: the simulated electric field at an instant of time compared to the theoretical ray showing good agreement. . 68

4.25 Total internal reflection at a glass (left) to air (right) interface of a single, planar wave 70

4.26 Mesh used for simulating a circular mirror and the first few waves of intensity from a Gaussian source. 71

4.27 (left) A comparison of three schemes from [17], (right) the same simulation using DGM. The horizontal axis represents the height on the screen, and the vertical is the amplitude relative to the incident wave. 72

4.28 Electric and intensity distributions at a fixed point in time of a Gaussian beam passing through a circular lens 73

4.29 (Saturated) average intensity of a Gaussian beam passing through a circular lens 74

Chapter 1

Introduction

1.1 Applications of Electromagnetic Simulations

Electromagnetics (also referred to as electrodynamics) is a large branch of physics which studies electromagnetic waves and signals (this includes light waves, radio waves and even x-rays) as well as electrical components and properties such as resistors, transformers, current and charge. Electromagnetics is invoked in the description of electrons firing down a copper wire and the construction of a perfect lens to minimize blur in a photograph. Needless to say, there is a very large range of simulations within computational electromagnetics.

Electromagnetism is, at its basis, the understanding of the electric and magnetic fields and their influence and reaction to the surroundings. There is a well known duality in electromagnetics, which gives us two ways of describing the underlying physics. The first, the wave description, relies on the definition of the electric and magnetic fields. In this approach, information propagates through the domain as electromagnetic waves in the two fields and we consider the medium through which the waves propagate on a macroscopic level. The wave approach is robust and reliable for macroscopic details of electromagnetics, but does not easily address the actions of individual photons such as absorption and the photoelectric effect. The alternative description of electromagnetics is through particles. It defines the electric and magnetic fields as the collection of electric and magnetic contributions from all the particles in that neighbourhood. This outline analyzes finite energy particles, i.e. photons, and traces their movement through the domain along specific paths known as rays. This approach is successful in explaining the individual events of photons interacting with other particles on tiny scales, but struggles to explain macroscopic phenomena such as interference. Both concepts have a place in physics, which has adopted the "wave-particle duality" of light, a theory which states neither theory of electromagnetics is complete without the other.

For the purposes of simulating electromagnetics, one is typically more interested in the wave concept since it is the better description of macroscopic properties of light and other electromagnetic waves. Furthermore, this description is captured in Maxwell's equations which can be addressed through the well established field of numerical solutions to partial differential equations. If desired, one could travel to an even more fundamental level and look at things on an atomic scale by analysing how elementary particles are behaving and looking at the quantum nature of electromagnetics. However, the classical Maxwell's equations offer a complete understanding of all systems besides those in the limit of very few photons or extremely high energy photons on exceptionally tiny domains. More formally, classical electromagnetics is sufficient as long as the momentum of a particular photon is small compared to that of the system, and the number of photons is large compared to those which may be spontaneously emitted from within the system [8]. To put this in perspective, the momentum of a high energy x-ray is of the same order as the momentum of a single electron; so as long as simulations are not modelling anything smaller than a group of electrons or more powerful than the strongest x-rays, we will be able to consider the momentum of each individual photon negligibly small. The second condition is satisfied in all but extreme cases as well. Spontaneous photon emissions can be either the result of radioactive atoms or blackbody radiation. Radioactive atoms are exceptionally rare in physical systems and only emit specific wavelength photons which would likely not be of importance in a given application. Blackbody radiation is always present but occurs at extremely low levels unless the system is heated to temperatures in the range of thousands of Kelvin (since Planck's law tells us the number of photons emitted from a blackbody is proportional to temperature to the fourth power).

Most important and practical problems in electromagnetics belong within the scale where the physics of fundamental particles need not be called upon. Microwaves, radar, medical imaging (x-rays), antennas and signal engineering, electric components, optics and optical devices are all governed by Maxwell's equations. However, even in the range of electromagnetics where we can safely neglect quantum electrodynamics, we have tremendous variation in the scale of the problems. The difference in wavelength between an x-ray and a radio wave is almost the entire range of electromagnetic spectrum, with a radio wave's wavelength being approximately 10^{13} times that of an x-ray. Furthermore, we could imagine being interested in simulations of light waves from the sun to the Earth, or we could be interested in focusing an x-ray or microwave into a volume of a few cubic centimetres. No numerical scheme can be optimized for such a diverse range of applications. This wide range of problems in electromagnetics has lead to development of specialized schemes which may be fast and accurate for a small subset of these problems but not applicable to the rest and general schemes which are widely applicable but inefficient for most problems.

The increasing performance of computers has had tremendous impact on the selection and development of numerical schemes. Prior to the 1990s, the relative lack of computing power left time domain simulations of electromagnetics as nothing more than a theoretical interest for almost all simulations since a sub-wavelength scale was simply not viable. During the 1990s a shift from more primitive methods to the finite difference time domain (FDTD) schemes and some even more advanced time domain schemes began [22]. These schemes offer a more general approach to computational electromagnetics, offering a wider range of physical problems which can be simulated at an increased computational cost. As technology improves, interest will shift to even more expensive simulations as long as they can offer improved accuracy or extend the range of possible simulations.

The historical motivation for computational electromagnetics was to perfect the art of constructing aircraft invincible to radar systems, but in the past two decades has found many new applications [40]. Simulations of electromagnetics at work in biological systems have been used to better understand experimental cancer treatments including electromagnetic hyperthermia [32] and to investigate how optical components of the human eye function [31]. More recently, techniques have been applied to the nanoscale physics to simulate plasmons and develop advanced nanoscale waveguides for light [26]. Numerical simulations are also frequently encountered in engineering applications such as antenna design and optimization [15, 17, 16].

1.2 Numerical Methods for Electromagnetic Problems

Besides the huge diversity of scales in electromagnetic problems, there is also a large variance in the degree of accuracy one may demand. For some problems it is sufficient to neglect the nonlinearities which arise in electromagnetics, or to trim off the fine details of the object in the middle of the domain, which allows the use of fast and simple schemes. Other problems demand a full solution with no simplifying assumptions; these typically require extremely expensive and complicated schemes.

In this work, we apply the discontinuous Galerkin method (DGM) to electromagnetic wave propagation. We do not focus on the simulation of conductive media where electric charge is mobile, or modelling specific electric components (although either of these is numerically possible), but instead are more interested in the propagation of electromagnetic waves in media such as air, glass, or even human tissue. This choice is aimed at applications including radio/microwave communications, optical lens design, and medical imaging. The DGM concept proves to be extremely general as, much like time domain finite element methods, the discontinuous Galerkin method does not restrict the types of electromagnetic systems we can approximate. The consequence of this is that the scheme is more complex than most and the computational cost is too high for problems on large domains with small wavelengths.

To understand the value of DGM, we begin by summarizing the other types of numerical schemes used in electromagnetics. The first alternatives are schemes which address problems in the frequency domain. These methods search for pseudo-steady state solutions for problems where this solution exists and is the primary interest. This assumption is somewhat restrictive since, although theoretically electromagnetic systems reach a steady state, the transient information is often not negligible and including nonlinearities (most notably non-uniform media) into these formulations will turn out to be extremely challenging. These methods typically employ a Fourier transform to obtain solutions since electromagnetic waves often have strictly sinusoidal terms (often with only one frequency) and periodic boundary conditions are very prevalent in electromagnetics. More complex boundary conditions and less ideal wave forms can introduce unwanted complexities into these schemes, but for well suited problems frequency domain analysis can be extremely effective [20]. These frequency domain solvers are effective for simulating a single frequency, however are unable to obtain broadband information in a single run. As a result, broadband analysis must be approximated with a finite combination of the involved frequencies, each simulated individually, or left to time domain schemes [3]. Both finite difference and finite element techniques have be manipulated to work in the frequency domain. In electromagnetics the term 'FEM' may refer to time or frequency domain schemes depending on the text, whereas finite difference is typically separated into 'FDTD' (finite difference time domain) and 'FDFD' (finite difference frequency domain).

One frequency domain scheme which has been particularly important historically, as well as today, is the method of moments (MoM), sometimes known as the boundary element method. This technique can be applied to integral equations, which are derived from Green's functions corresponding to the induced electromagnetic fields from every element of surface charge on all surfaces within the simulation. MoM is well developed for standard electromagnetic problems and geometries, however, dealing with complex geometries will become difficult as it requires derivation of customized Green's functions for all irregular boundaries. The simulation times of MoM can also become enormous since, if one wishes to sample the electric field at N points in the domain, this leads to a solving a densely populated $N \times N$ system of equations [34]. In fact, the situation becomes very unfortunate when one considers that to get reliable resolution in three dimensions, one usually needs to choose

$$N > 600\frac{d^2}{\lambda^2} \tag{1.1}$$

where d is the length of the object being illuminated and λ is the illuminating wavelength [40]. Furthermore, the matrix operations involving the dense NxN system generally include an LU factorization, putting the order up to N^3 or, equivalently, depending on frequency to the sixth power.

Secondly, there are many schemes that make use of the particle theory to treat light waves (and other electromagnetic waves) as rays with predictable (or statistically predictable) behaviour. Rays represent another way to understanding the electromagnetic distributions within a domain. Each ray represents the direction of the flow of radiant energy coming from some source [18]. These paths always run perpendicular to the wavefronts of the electric and magnetic fields. The first of these methods are known as geometrical optics (GO). These schemes are extremely fast and effective for problems with large domains. Since GO schemes use a point-and-shoot algorithm, the computational time is hardly affected by the size of the domain. Furthermore, using the ray analysis means that changing the frequency of the waves also has next to no impact on the runtime of the algorithm and electromagnetic parameters of the medium can easily be defined with dependency on the frequency. Both of these features directly contrast with the negatives of the more general schemes which make these methods effective for hybridizing. GO schemes are usually improved through means of upgrading the decisive ray behaviour to a statistical behaviour through Monte Carlo simulations. In fact, there are powerful software packages commercially available which can model complex systems like this (LightTools and POV-Ray for example). However, for a complete simulation, GO schemes need to incorporate many correction factors for the large number of possible phenomena electromagnetic waves are capable of. Some of these, e.g. total internal reflection and refraction, are straight forward to implement. Others, e.g. partially diffuse surfaces and scattering, become much more complex and require Monte Carlo simulations as well as a lot of experimental data from the specific media or surface. A historically significant extension to GO techniques is the geometrical theory of diffraction (GTD) which was developed to include diffraction somewhat mechanically through predetermined diffraction coefficients [23]. GTD was one of the dominant schemes prior to the exponential growth of computer power, however it was severely limited by documented defects including nonphysical field infinities at focal points, caustics, and shadow boundaries [42]. GO and GTD schemes also lose a lot of their computational efficiency if the user attempts to investigate interference since it vastly increases the required memory. These schemes are often categorized as high-frequency methods, since they rely on assumptions and approximations which are more accurate at higher frequencies. As such, these schemes are most frequently applied to optics since light waves are high frequency waves but GO and GTD are also viable for other high frequency electromagnetics such as x-rays. Schemes using ray-tracing such as these are considered diffraction-limited since they only converge in the $\lambda \to 0$ limit where diffraction and interference do not exist. To add to the list of flaws, these techniques require an extreme amount of reworking to remain accurate in cavities and waveguides or anywhere else where rays bounce repeatedly [42].

Next, an improvement on GO techniques, known as physical optics (PO) schemes, incorporates wave optics in addition to the GO concept. These methods typically operate by running a ray-trace scheme to calculate the distribution on an interface and use this knowledge to determine the induced surface charge. One can then integrate the influence each part of the surface contributes to the total reflected or scattered field from this interface [43]. PO methods also require numerous correction factors to calculate how much of a wave may be scattered, diffracted, absorbed, and transmitted. Just as the GTD was developed, a parallel physical theory of diffraction (PTD) exists and is an improvement to PO schemes allowing them to incorporate diffraction at specific, important regions [41]. The fundamental assumption for these schemes is that the wavelength is short so that the ray optics to calculate the incidence waves onto an interface are accurate and the induced surface charge is predictable. These schemes run into difficulties for large wavelengths, as well as small objects and more complex surface materials which may feature challenging induced surface charges. In addition, more precise and costly schemes are sometimes required to get accurate estimates on some of the coefficients needed for the scheme. These coefficients often vary with wavelength which can further diminish the usefulness of PO schemes for some applications.

To further improve the numerical approximations, mathematicians, physicists and engineers often turn to directly applying numerical schemes to Maxwell's equations. This idea bypasses any approximations on the wavelength at the cost of sacrificing the huge acceleration these constraints were able to provide. Maxwell's equations form a system of partial differential equations suitable to be solved by methods such as finite difference and finite elements. Since these solutions are not done in the frequency domain they are known as time domain solutions, examples include: FDTD (finite difference time domain) and FETD (finite element time domain, also known as simply FEM). These methods yield large algebraic systems to be solved, but, unlike the MoM, the matrices involved are sparse and typically almost exclusively populated along a small number of diagonal bands. The leap into direct time domain simulations is often credited to Kane Yee, who was amongst the first to apply FDTD. In fact, FDTD applied to Maxwell's equations is sometimes called the Yee Algorithm, particularly when the electric and magnetic fields are collected on respectively staggered grids as he proposed [45]. FDTD is rather well established but does have some problematic features. Most noteworthy of these issues are the anisotropic error in propagation speed [6] and the difficulty to fit curved boundaries into a scheme heavily reliant on a square grid. Finite element and, to a lesser extent, finite volume codes have also been used however are seen less frequently than FDTD, likely a consequence of the increased computing power required to use them. The discontinuous Galerkin method falls into this category and is most closely related to FETD.

Time domain schemes solve the problem on a meshed domain. Since a larger domain requires either more or larger elements, increasing the size of the domain means that the numerical solver must sacrifice speed or resolution. Furthermore, these schemes will find high frequency waves to be particularly challenging to model since the small wavelengths forces a restrictive condition on element size, which in turn quickly increases the computational runtime. Failure to create elements small enough for the given wavelength will introduce numerical diffusion into the simulation which will quickly reduce accuracy. As a result, time domain schemes are generally only applicable to problems where the wavelength is not excessively small compared to the size of the domain. A clever approach to this issue which has been proven to be successful involves hybridizing schemes. This is usually achieved by applying a simple technique such as GO or PO to most of the problem domain, and using time domain (or frequency domain if possible) methods to regions where fine detail is required around relatively small objects [15, 28].

In this work we analyze and demonstrate the applicability of the discontinuous Galerkin method to problems in electrodynamics and closely examine what value this alternative may possess. Beginning with the simplified case with many assumptions and restrictions on the set of problems we may solve, we then relax these requirements and expand the range of this scheme to a relatively broad set of simulations while maintaining the benefits of the DGM. Discontinuous Galerkin methods have been shown to fit into the electromagnetic framework in [19], and have been applied to some examples in [12]. However, the implementation is typically limited to reasonably simple simulations. The reason for this may simply be that computational resources are just recently breaking the barrier that makes transitioning to time domain FEM and DGM a potentially worthwhile investment. Here, we investigate the potential range of problems this method is suitable for and simulate a sample of these applications. We also seek to expand the types of problems DGM can handle by deviating from the simplest cases in computational electromagnetics while maintaing a very general framework for our scheme instead of including specific corrections.

1.3 Maxwell's Equations and the TM mode

All macroscopic, electromagnetic phenomena are governed by a set of partial differential equations known as Maxwell's equations. These equations are the centrepiece of the wave theory for electromagnetics which includes the formation of electric and magnetic fields by charges and current, as well as the propagation of an electromagnetic wave from an oscillating source or some initial disturbance.

Maxwell's equations appear in many different forms through assumptions and simplifications, however, they are always presented as four partial differential equations involving electric and magnetic fields

$$\frac{\partial \vec{B}}{\partial t} + \nabla \times \vec{E} = 0 \tag{1.2a}$$

$$\nabla \cdot \vec{D} = \rho \tag{1.2b}$$

$$\frac{\partial \vec{D}}{\partial t} - \nabla \times \vec{H} = -\vec{J} \tag{1.2c}$$

$$\nabla \cdot \vec{B} = 0. \tag{1.2d}$$

These equations are known individually as Faraday's law, Gauss's law, Ampère's circuital law (with Maxwell's modification), and Gauss's law for magnetism respectively. The variables $\vec{E}$ and $\vec{H}$ represent the electric and magnetic fields, while $\vec{D}$ and $\vec{B}$ are the electric displacement and magnetic induction. ρ represents the electric charge density, and $\vec{J}$ the electric current density.

In this work, we assume we will be modelling linear, isotropic and nondispersive media. These three assumptions are not very restrictive since most media of interest for electromagnetic wave propagation fit into this category very well. These assumptions allow us to apply the following constitutive relations

$$\vec{D} = \epsilon \vec{E} \tag{1.3a}$$

$$\vec{B} = \mu \vec{H}. \tag{1.3b}$$

Here ϵ is the electric permittivity of the medium, and μ is the magnetic permeability of the medium. These two parameters are collectively known as the electromagnetic coefficients of a medium.

A medium is said to be linear if its polarization responds linearly to an applied electric field. This is true for dielectric materials such as air and glass. Media which are not linear have interesting electromagnetic effects such as those of ferromagnets or ferroelectrics.

However, all media can be considered linear for small signal ranges [37]. Furthermore, extremely intense electric fields can cause electric breakdown of the material which will destroy the linear response, but these intensities are limited to events such as lightning and are not observed in electromagnetic waves propagation problems like those in optics or signal transmission. Incorporating nonlinear media into the formulation would be challenging for most schemes since the value of ϵ and μ would depend on $|\vec{E}|$ and $|\vec{H}|$, which would make the system of partial differential equations nonlinear and, hence, more complex.

Isotropic mediums propagate information at equal speeds in all directions, and are much more common than the counterpart, anisotropic media. The generalization to include anisotropic media appears to be very straightforward, since it would simply require replacing the constants ϵ and μ with 3×3 matrices. However, it is noted in [29] that although the finite element (and DGM) framework can be generalized to handle anisotropic media, this process can add in much complexity and makes the convergence results difficult to prove. However, uniqueness of the solutions to Maxwell's equations has been proven in this case in [44].

And lastly, although most media feature some dispersion, if we assume we are using a small range of frequencies the assumption that all the waves in the system have the same speed is valid (exact if we are only using one frequency). This fact is illustrated in [18] where they demonstrate that over the range of 388nm to 728nm wavelengths (roughly the range of all visible light) the wave speeds are within 1.5% in crown glass. So, little dispersion is present over a relatively large variation in wavelength. Incorporating dispersive media into the formulation adds an interesting nonlinear effect since the coefficients ϵ and μ depend on λ which is derived from the electric (or magnetic) field. This can be incorporated into a numerical scheme through a spectral analysis (which will have to be performed every time step) or can be approached similarly to how methods like MoM handle multiple frequencies - by simulating them one at a time. Either of these approaches can be used for time domain schemes but may add expensive steps to the process.

These constitutive relations (1.3) allow us to work with the following version of Maxwell's equations

$$\mu\frac{\partial \vec{H}}{\partial t} + \nabla \times \vec{E} = 0 \tag{1.4a}$$

$$\nabla \cdot \vec{E} = \frac{\rho}{\epsilon} \tag{1.4b}$$

$$\epsilon\frac{\partial \vec{E}}{\partial t} - \nabla \times \vec{H} = -\vec{J} \tag{1.4c}$$

$$\nabla \cdot \vec{H} = 0. \tag{1.4d}$$

The equations (1.4a) and (1.4c) form a hyperbolic system of partial differential equations (the other two do not need to be modelled as explained in Section 3.5). These equations are hyperbolic because, if re-expressed as

$$\vec{u}_t + \mathbf{A}\vec{u}_x + \mathbf{B}\vec{u}_y + \mathbf{C}\vec{u}_z = \vec{s} \tag{1.5}$$

where $\vec{u}$ contains $\vec{E}$ and $\vec{H}$, then the matrix $a\mathbf{A} + b\mathbf{B} + c\mathbf{C}$ is diagonalizable for any choice of a, b, c. This is shown for Maxwell's equations in two-dimensions in Section 3.3 where we show that this 3×3 matrix has three unique eigenvalues, which makes it diagonalizable.

Furthermore, the system of equations (1.4) are very closely tied to the wave equations. Under certain conditions Maxwell's equations directly lead to the wave equations for the electric and magnetic field. This connection is demonstrated in [8] where it is shown that in the types of media we discussed above, with the additional assumptions of a source-free, nonconducting medium, Maxwell's equations can be reformulated exactly into the wave equations

$$\nabla^2 \vec{E} = \epsilon\mu \frac{\partial^2 \vec{E}}{\partial^2 t} \tag{1.6a}$$

$$\nabla^2 \vec{B} = \epsilon\mu \frac{\partial^2 \vec{B}}{\partial^2 t}. \tag{1.6b}$$

The extra assumptions tell us that since there are no source terms, $\rho = 0$ (no charge) and $\vec{J} = \sigma\mathbf{E}$ (Ohm's law). Furthermore, a nonconducting medium has a conductivity of $\sigma = 0$. The consequence of this is that, in this ideal medium, electromagnetic waves travel according to the wave equation with speed $c = (\epsilon\mu)^{-0.5}$ as expected. In fact, some electromagnetic simulations are applied to these wave equations. This is avoided here because it restricts some features from being simulated. The analysis done here concerns itself with the function of Maxwell's equations to represent solutions of propagating waves through non-trivial domains. We are most interested in nonconducting media, since this is where wave propagation happens, so we assume that $\vec{J}$ does not depend on $\vec{E}$. At this point we can say we are working with linear, isotropic, nondispersive dielectric media.

Maxwell's equations produce a number of other interesting features in well behaved dielectrics. Electromagnetic waves always travel at a fixed speed in a given medium, known as the speed of light, and given by

$$c = \frac{1}{\sqrt{\epsilon\mu}}. \tag{1.7}$$

Electromagnetic waves also have the property that the electric field and magnetic fields are orthogonal in three dimensions, and that the direction of propagation is equal to the cross product of the two fields. Although full three dimensional modelling is a possibility, working in two dimensions allows for a much faster and often more interpretable results. There are two standard choices for two dimensional electromagnetics, and we choose the transverse magnetic (TM) mode. This is characterized by an electric field pointing orthogonally to the domain, and the magnetic field and wave propagation being in the plane. The alternative choice, which is also suitable for simulations, is the transverse electric (TE) mode, which is similar but with magnetic and electric fields switched.

Chapter 2

DGM Concept for Electromagnetics

2.1 Why DGM?

Possibly the most distinct feature of the DGM is its capability to handle discontinuities and steep gradients in the solution very well. Where other schemes may produce large, unwanted oscillatory errors near a discontinuity or rapid changes in the function value, DGM prevents errors from propagating throughout the system and does a good job at properly resolving the tricky distribution. This is important to electromagnetics in at least two situations. First, electromagnetic waves are capable of creating focal points and caustics when interfering with mirrors or lenses, both of which produce rapid changes in the intensity of the field strengths and can be tough to simulate accurately. Secondly, the electric and magnetic field strength is, in general, discontinuous across an interface with a changing index of refraction [38]. Although this forms a static discontinuity which may be less troublesome to numerical schemes than a travelling shock, it is still valuable to have a scheme which can innately handle this situation.

The DGM is fundamentally similar to FETD techniques; as such it has a lot of the same benefits. It also has approximately the same computational cost, making it relatively time consuming compared to other methods. However, unlike FETD, the mass matrix is local since all basis functions are defined only on a specific cell. This causes the mass matrix to be very easy to invert and handle, whereas the FETD mass matrix increases with the number of cells and can lead to extremely time consuming calculations. Furthermore, the locality of the DGM scheme makes it highly parallelizable. This can potentially offer a significant speed up which is a very desirable feature particularly for costly methods such as DGM [10]. The fact that DGM uses strictly local basis functions will make the process of parallelizing the code relatively easy and powerful since large components of the algorithm are done individually on each element anyways. As with FETD, the DGM is capable of handling nonlinear equations which is a large difficulty for frequency domain schemes.

The DGM also features a customizable numerical flux, which is not present in FETD. The numerical flux can be a time consuming feature of the scheme, however, it allows more flexibility to ensure stability for wave-dominated problems such as electrodynamics [19]. As with FETD, the DGM works on a non-uniform mesh, which can conform to any geometry and even include curvilinear elements. This is a very important feature for electromagnetics since it immediately bypasses the two largest problems of FDTD: direction dependant error in velocity and difficulty modelling boundaries that do not fit directly into a Cartesian mesh. The mesh can be locally refined and, if desired, can utilize adaptive mesh refinement.

The DGM used in this work approximates a solution to Maxwell's equations within the time domain. The time domain calculations are different from frequency domain or asymptotic techniques (such as ray tracing) since they offer a more complete data set and the opportunity to simulate mediums with extremely complex electromagnetic features and geometries such as human tissue. However, the time domain data set is much larger and the system may take a large number of time steps to reach its final state making the schemes more expensive. Compared to the method of moments, with modern computing power we are able to simulate larger system to wavelength ratios with time domain schemes because of the very poor convergence of MoM [42]. But, other frequency domain schemes and certainly ray-tracing options will be able to simulate larger domains with smaller wavelengths.

For the DGM to be applicable at all we require the standard results on convergence and stability for the DGM. Fortunately, these have been proven, even for higher dimensions, in [9]. If we define h as the radius of the (largest) inscribed circle within the triangular elements, and p as the order of our basis, and assume that our triangulation is quasi-uniform, it has been proven that this convergence satisfies the relationship that the norm of the error is of order $h^{p+\frac{1}{2}}$ for linear problems. In this context the norm used is a broken norm, which is defined as the square root of the sum of all the squared inner products on each element. This result has been improved to the theoretical order of convergence of one dimensional DGM, $O(h^{p+1})$, provided the grid is quasi-uniform and that all edges are bounded away from the characteristic direction [19]. In practice, the observed order of convergence of the DGM in higher dimensions is $O(h^{p+1})$.

2.2 Boundaries and Surfaces

There are several behaviours an electromagnetic wave may display upon contact with a boundary. If the boundary is an interface of two mediums capable of transferring the electromagnetic wave, some of the wave may enter the new medium and refraction will occur. Refracted waves appear to bend or change direction upon entering the new medium. They also change speed. Depending on the electromagnetic coefficients, reflection may occur. The reflection may be specular, as is the case of total internal reflection from under the surface of water or a reflection from a perfect mirror. Specular reflections obey the law of reflection which states that the angle of reflection equals the angle of incidence. However, the reflection may also be diffuse, where the reflection acts like a new point source at the location the wave struck the boundary. Diffuse reflections may be perfectly uniform, this is known as Lambertian reflectance, where the output from each ray is a uniform hemi-sphere from the point of contact. The diffuse reflection may have a non-uniform distribution of reflected waves as well. Surfaces also typically absorb some of the incident energy, resulting in the energy leaving the system by other means, generally heat. Perfectly absorbing surfaces are known as black bodies as none of the light (or other electromagnetic radiation) is recovered once it strikes the surface.

In reality, surfaces usually exhibit a combination of these effects. Most surfaces are not ideal reflectors, but reflect more light along the direction of the geometrical reflection than in other directions; this also suggests most surfaces are not uniform diffusers. Reflections are always accompanied by losses due to absorption; however, for a good mirror the component of energy lost is extremely small. The picture becomes even more complex when the medium on the other side of the interface allows the propagation of light. In such cases a lot of energy is passed through the interface, causing refracted waves in the second medium. How much of a wave is transmitted and how much is reflected depends on the electromagnetic coefficients of the two media as well as the polarization of the incident light waves.

In the discontinuous Galerkin method, boundary conditions are handled via ghost states which are imaginary values used just outside of the domain to give us the desired effect on the boundary. Time domain schemes in general require the use of ghost states or ghost cells, using ghost states is advantageous since it does not require any extra storage and typically only an extremely minimal computational effort. Reflections are handled by having the same information in the ghost state except for the velocity which is transposed over the boundary. However, this is slightly more complex since velocity is not a variable for Maxwell's equations. Instead we will transpose the magnetic field over the normal. This will yield the same results through the property of electromagnetics that the direction of propagation is given by the cross product of $\vec{E}$ and $\vec{B}$. We assign the ghost state a value which has the same electric field and value of $\vec{B} \cdot \vec{n}$, but the cross product $\vec{B} \times \vec{n}$ is negative the value just inside the domain. The exact formula for such a ghost state is given in Section 3.4 by equation (3.48).

Lambertian or diffusing surfaces exist due to imperfections in the flat surface (or the lattice structure if the waves penetrate the surface). If we think of light as emitting a spherical wavefront from each point along the current wavefront (this description of an electromagnetic wave is known as Huygen's Principle [18]), it becomes understandable that the laws and equations for specular and diffuse reflection are in fact the same. The difference comes as a consequence of differences in surface geometry, so the most complete model of reflection does not require a different functionality for specular versus diffuse surfaces, but the capability to handle very complex surface geometries.

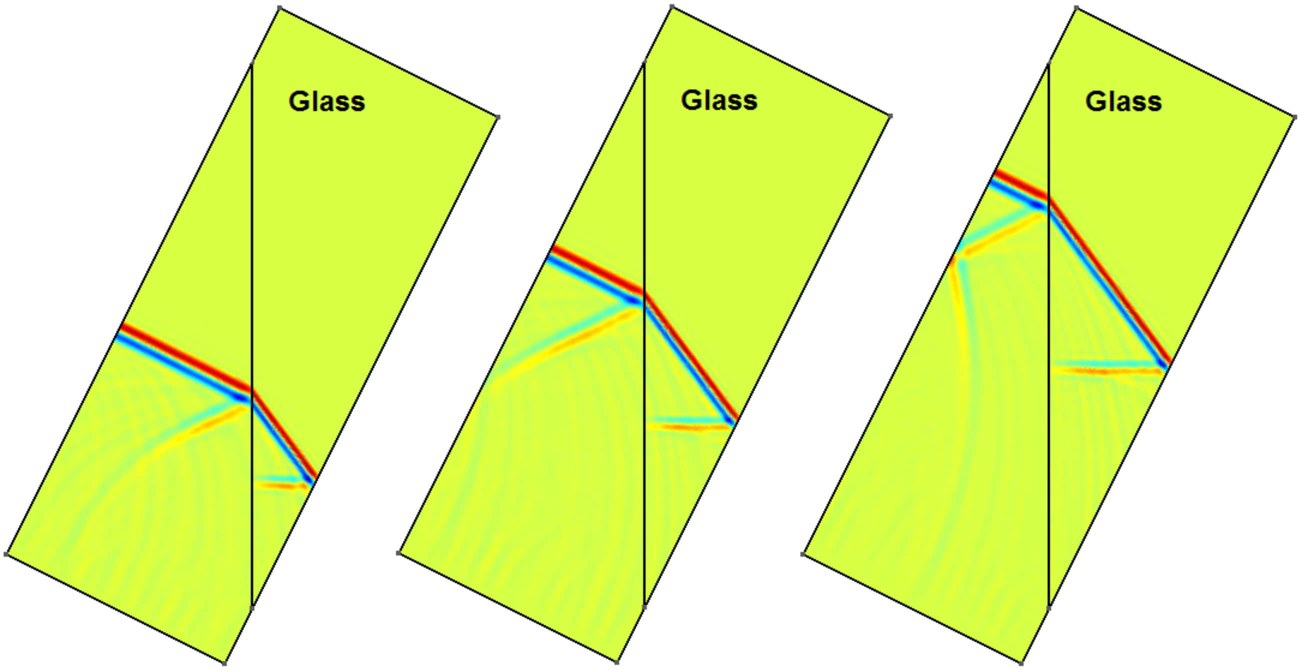

Figure 2.1: A single wavelength of a sine wave initiated in air interacting with a glass wedge, showing various types of reflections

Boundaries between two different media which allows transmission usually features some reflection, the quantity of which is determined by the Fresnel coefficients which are functions of the angle of incidence and indices of refraction. One benefit of a direct simulation of Maxwell's equations instead of the wave equation or ray tracing is that this feature is naturally implemented in the time stepping scheme. Furthermore, through the use of Maxwell's equations the correct phase change effects are observed in these reflections. For instance, the phase change from a total internal reflection depends on the angle of incidence, and the Fresnel reflection from a less optically dense medium such as air into a denser one, like glass, is always a full 180 degrees. Lastly, reflections from perfect mirrors feature no phase change. These features become complex to implement individually, especially when they depend on a number of parameters such as angle of incidence.

The images in figure 2.1 illustrate many of these effects. A plane wave originating in air strikes a wedge of glass at a large angle of incidence. The air-glass interface is along the vertical line in the middle of the domain. Most of the light is transmitted into the glass but some experiences a Fresnel reflection at this interface. The reflected wave undergoes a perfect 180 degree phase shift which causes the incident wave of a positive peak followed by a negative peak to change into a reflected wave featuring the peaks in reverse order. This reflected wave will later strike the left boundary, which is a perfect mirror. The mirror will induce no phase shift when it reflects this wave (the wave is no longer be planar here as a result of diffraction). Lastly, on the right boundary, the transmitted wave changes its angle of propagation due to refraction then strikes a glass-air boundary which results in total internal reflection. In this instance the angle of incidence is very large (near tangential to the boundary) so the phase change in this total internal reflection is nearly a full 180 degrees. Later, in Section 4.5 we will examine a simulation designed specifically for total internal reflection and will see a more characteristic phase change between zero and 180 degrees. When performing these simulations with the DGM, or other time domain schemes working directly on Maxwell's equations, these phase changes are accurately produced by the schemes.

2.3 Diffraction

Diffraction is sometimes defined as the deviation of light from rectilinear propagation (as stated originally by Francesco Grimaldi in the 1600s). Although the exact definition of diffraction and interference are somewhat overlapping, it is customary to refer to diffraction as the effects of many light waves at once - such as the bending of a plane wave around a corner. Interference is used to describe situations where only a few waves are interacting with each other. Diffraction is an effect present in all electromagnetic waves, but is most recognizable when those waves are visible light. For this reason diffraction is sometimes said to be a feature of light, but it does in fact apply to electromagnetic waves of any wavelength.

Diffraction is a phenomenon where the shortcomings of ray or geometrical optics are most evident. It is also an important feature of electromagnetics which is responsible for a lot of complexities. It often makes fascinating and unexpected distributions on small scales (relative to the wavelength of the electromagnetic radiation) however is also responsible for features and loses in larger systems.

The presence of diffraction in Maxwell's equations can easily be shown by the realization that a plane wave with constant amplitude along the wavefront cannot be a solution unless the plane has infinite length in all directions orthogonal to propagation. This rectilinear propagation is the theoretical solution one arrives at through geometrical optics but is only a theoretical solution as we let the wavefronts width tend to infinity.

There are many experiments which confirm the deviation of real wave propagation from simple geometrical optics predictions. The most common examples of this are the single and double slit experiments (often named after Thomas Young who originally performed them) and the effect of diffraction gratings. All of these experiments produce light and dark bands due to interference some distance away from the aperture placed in front of a (theoretically) plane wave. Diffraction explains the bending of electromagnetic waves, whether it be around a corner or just the fact that these waves propagating through free space will change shape rather than act like solutions to the advection equation. Diffraction is well explained through the Huygens-Fresnel principle; which states that every point on the wavefront, at each given instant, acts like a point source emitting a spherical wave. The theory explains that the correct electric field can be found at the next instant in time by considering the input from each of these point sources (incorporating phase) at the present instant.

We witness diffraction all over the place, from rainbows to the divergence of a flashlight or laser beam. A clear display of diffraction occurs when a perfect plane wave strikes an aperture, allowing only a centre component of the wave through. The part of the wave which passes may look like a plane wave for an instant however quickly begins to shed intensity to either side, effectively allowing light waves to 'bend' around this object. These diffracted waves are not as strong as the plane waves, however they are important in many situations and they also reduce the energy of the central plane-like wave as a consequence of the conservation of energy. We see this effect happening in figure 2.2, but we also see a less intuitive consequence of Huygens-Fresnel principle: a strange interference pattern appears not only within the forward propagating plane wave, but also in the plane waves prior to the aperture. This can be seen in the elevated plot and is the result of the unbalanced spherical waves coming from the edges of the aperture. If the aperture was not there, these ripples would be cancelled out by the influence from the neighbouring points which would not have been blocked out. This strange extra feature is sometimes referred to as the boundary diffraction wave.

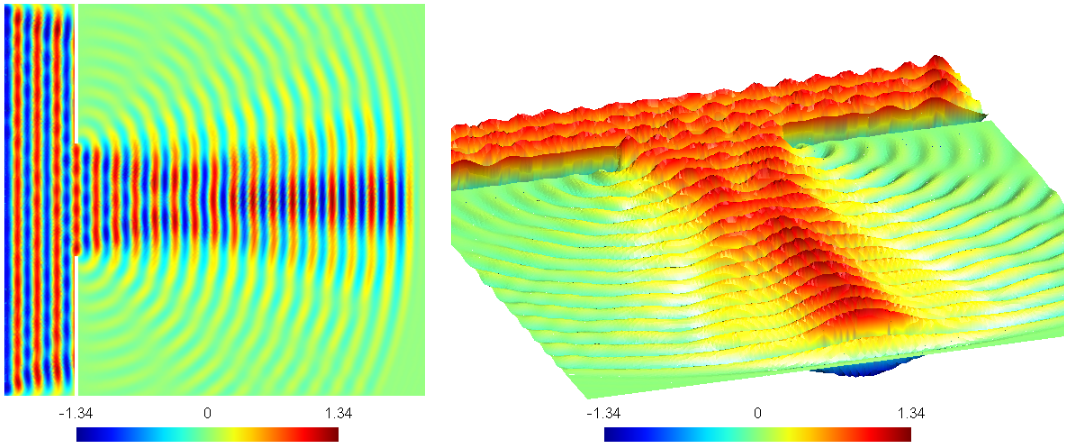

Figure 2.2: Plane waves originating at the left boundary strike an aperture as depicted in left figure. Diffraction occurs causing the plane wave to seemingly wrap around the edges of the aperture.

Diffraction is a feature which makes exact solutions to Maxwell's equations extremely challenging to obtain. For this reason, most theoretical solutions use either Gaussian beams or idealized plane waves where the effects of diffraction are minimized. Gaussian beams feature the property that, although they will spread out, they maintain a Gaussian profile but with an increasing (or decreasing) beam width as they propagate. A Gaussian beam is often characterized by its beam width, the measure of how far from the centre (in the direction orthogonal to propagation) the amplitude decays to $\frac{1}{e}$ of the central amplitude. The beam waist is the minimum value for this width and is denoted by ω_0. At a distance x from the beam waist, the beam width is given by

$$\omega(x) = \omega_0\sqrt{1+\left(\frac{\lambda x}{\pi\omega_0^2}\right)^2} \tag{2.1}$$

and the Gaussian profile of the intensity is given by

$$I_z(x,y) = I_0 e^{-\frac{y^2}{\omega(x)^2}}, \tag{2.2}$$

where I_0 is the peak intensity at the beam waist [7]. When a Gaussian beams travels through a lens it can be altered to change from a diverging to a converging beam and can also adopt a new value of ω_0 as is seen in Section 4.6. In figure 2.3, we initialize a Gaussian beam at the centre of the domain to demonstrate its behavior as it radiates outwards in both directions from the beam waist at $x = 0$, where the source of the waves are.

Gaussian beams are also of practical interest because many laser beams operate in the most fundamental mode (known as the transverse electromagnetic 00 mode or TEM_{00}) which has a Gaussian distribution in all directions orthogonal to propagation [18].

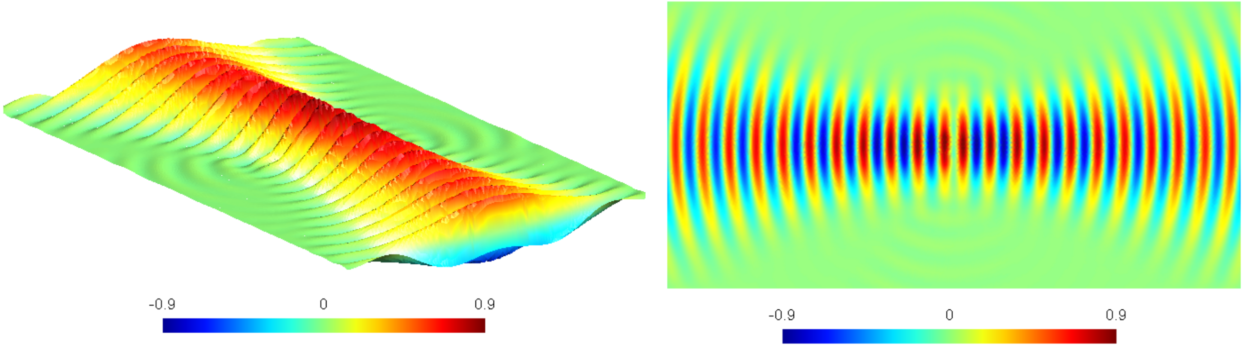

Figure 2.3: A Gaussian beam propagating in both directions from the the Gaussian source at x=0 in the middle of the domain.

Plane waves can be simulated by either making an extremely long plane wave initially (so that the centre portion remains roughly planar) or through implementing reflective or periodic boundary conditions to emulate an infinite width plane wave. In our simulations we use the latter as it is computationally much more effective, however requires care to be taken that these reflective boundaries are not influencing the simulation in unwanted ways.

2.4 The Practical Range of DG

Like FETD, finite volume, and FDTD, the DGM works on a mesh which must be fine enough to resolve the features in the solution, otherwise expecting a reasonable level of accuracy is impractical. Having to solve the equations on more elements makes these schemes more accurate and reliable but will increase the time required to run the simulation. This time requirement can make some simulations out of reach for time domain schemes. Fortunately, the only real limitation which may make DGM inapplicable to any problem is the required runtime.

Assuming our incident waves will have a known characteristic wavelength, we can predetermine the size our mesh elements need to be to accurately capture the behavior from these waves. It is important to take into consideration that the system can produce wavelengths shorter than these incident waves if reflections are present or if the waves will enter media with lower wave speeds. However, these effects are also easily predetermined with some minor insight into the solution. Obviously, smaller cells will better resolve the waves, but will also become more costly to run simulations. Depending on the order of the basis functions we allow on each cell, the number of cells needed to accurately resolve the waves will vary as well. For example, with only first order basis functions we need to have at least ten cells per full wavelength for good resolution, whereas for a third order basis we can relax this requirement to around four cells.

Eventually, creating cells smaller than a certain size becomes too time consuming to simulate. So, if we try using very small wavelengths, the DGM has to be run on an increasingly fine mesh and becomes increasingly expensive. This can be counteracted somewhat by increased computational resources or allowing longer run times, but these extensions offer a finite improvement of the range of wavelengths we can simulate using DGM which will certainly fall short for some applications.

On the more time consuming end of simulations run so far is the example presented in Section 4.6 which features a domain of 15 by 15, with 3.5 radius lens in the centre. The wavelength in this simulation was then 0.35 and we used a third order basis to obtain good resolution of these waves. Note that these are all dimensionless units since the simulations are all scaled. In this application we examine a wavelength which is 2.3 percent of the characteristic length of the domain, if we imagine a domain of size 15cm to be of interest for some application - this corresponds to a wavelength of 3.5mm which would be in the extremely high frequency band of the electromagnetic spectrum. This region of the spectrum includes the shortest radio waves, better known as microwave radiation.

If instead the domain was 15mm by 15mm we would be investigating 0.35mm wavelengths which fall into the range of Terahertz radiation, just slightly longer than the longest infrared waves (conventionally described as 0.3mm long). We could also improve the ratio of 2.3 percent of the length of the domain by decreasing the height of the domain, using lower resolution in regions of less interest, or allowing the simulation run for longer. Also, since DGM is capable of *hp*-refinement, we can increase the order of the basis on each element (*p*-refinement) and relax the *h*-refinement to allow larger cells. This practice typically results in a net increase in performance, and is demonstrated for low order basis in Section 4.1. Factoring all of these considerations in, dropping down to well below one percent of the domain length is surely possible, and with improved code more tailored to a specific problem, parallelization, faster machines, and GPU computing - going quite a bit below that is certainly achievable.

Working with an obtainable limit of one percent of the domain length, if we wanted to simulate visible light with this technique, we would be restricted to a domain size of one hundred times the approximate 500nm wavelength of light. This domain would be on the order of 50μm - approximately the width of a human hair. As such, applying DGM (or any of the similar time domain alternatives) is not practical to visible light within the time domain for anything but tiny scales (pending the development of even faster machines or more parallelized coding). However, these techniques are viable approaches for anything longer than infrared which includes radio waves, microwaves, terahertz radiation, and even infrared radiation on sufficiently small domains.

The question remains, are these wavelengths worth studying? Fortunately, this part of the electromagnetic spectrum falls within a demanding area of research. Radio waves are obviously experienced quite frequently even in daily life, everything from the electric field surrounding overhead power lines and other electrical circuits to the signals received by car and television antennas as well as radar detection (which some consider microwave frequency). Microwaves have the famous household use of a microwave oven, which is actually a consequence of a microwave photon being able to excite components of the small, polar water molecules causing them to vibrate and rotate leading to the release of energy as heat [14]. Microwaves are also applied to some radar applications, garage door openers, wireless telephone signals and even have applications in deep space exploration [18]. Slightly shorter than microwaves, waves in the terahertz region have interesting applications including airport body scans, skin cancer detection, dental imaging, and pharmaceutical quality control [17]. Infrared radiation is absorbed and emitted through thermal agitation of virtually all molecules, it also finds practical applications in medical imaging and treatments, laser beams for heating, cutting and cauterizing, as well as heat seeking missile technology [18]. A lot of these applications are worth simulating, perhaps most notably radar and antennas for optimization of engineering design.

Chapter 3

Discontinuous Galerkin Formulation for Maxwell's Equations

3.1 Meshing

We begin with standard triangular meshing. Cartesian or other meshes can also be used in the DGM, but triangles are generally advantageous when fitting a mesh to a complex geometry. The mesh plays a very large role in determining the trade-off between efficiency and accuracy of the simulation. Besides the obvious consequence of more cells increasing accuracy while increasing run time, the structure of the mesh also determines the Courant-Friedrichs-Lewy (CFL) condition.

The CFL condition restricts the size of time step we are able to use while maintaining stability of the scheme with explicit time integrators. In practice, the choice of time step is determined by the CFL condition, to maintain stability, rather than accuracy concerns from the time integration. In [11], it is demonstrated that a CFL condition of

$$\Delta t \leq \frac{\Delta x}{c_{max}(2p+1)} \tag{3.1}$$

must be satisfied for the (one dimensional) DGM with time step Δt, element width Δx, basis functions of order up to p, and maximum speed of propagation c_{max}. This is assuming one uses a Runge-Kutta time integration scheme of order $p+1$. In two dimensions, we take Δx_j to be the radius of the inscribed circle within element j. We then use h (which is the higher dimensional replacement for Δx) to be the minimum value of Δx_j.

The code can also be optimized by carefully minimizing the area which needs to be meshed. By cutting out regions which are not important, we can reduce the number of cells and decrease the runtime without affecting accuracy. Furthermore, since DGM does not require a uniform mesh, we can improve efficiency by placing more cells in regions where higher resolution is required and fewer (but larger) cells in regions where a high resolution is not necessary

Since DGM is a conservative time stepping algorithm, adaptive meshing can be performed by breaking down and merging cells between time steps. Although this does have some cost, it can increase accuracy without increasing the computing time as much as globally refining the mesh. When this process is used, the CFL condition may demand that the time step either changes over time or is defined conservatively for the smallest possible cell. It is also possible to adaptively change the order of the basis on specific cells if desired.

The choice of element size also effects numerical dispersion and diffusion. For the DGM, numerical dispersion and diffusion are of order h^{2p+2} and h^{2p+1} respectively [2, 21]. In the simulations performed on Maxwell's equations we never detected any significant dispersion, however, for poorly refined meshes with low values for p, diffusion heavily influenced the system. As the condition on diffusion predicts, increasing the order of the basis used or refining the element size quickly cleared up the numerical diffusion as shown in Section 4.1

3.2 Formulation

We begin by developing the transverse magnetic formulation of Maxwell's equations which is the two dimensional form of the equations we wish to compute numerical solutions for. We will define our solution to be on the x-y plane, so we can write $\vec{E} = (0, 0, E_z)^T$ and $\vec{H} = (H_x, H_y, 0)^T$ in accordance with the statement in Section 1.3. Of the four partial differential equations, we need only simulate two of them since the other two will be satisfied automatically (as long as our initial conditions are properly defined, see Section 3.5). The two equations we model are

$$\mu \frac{\partial \vec{H}}{\partial t} + \vec{\nabla} \times \vec{E} = 0 \tag{3.2a}$$

$$\epsilon \frac{\partial \vec{E}}{\partial t} - \vec{\nabla} \times \vec{H} = -\vec{J}. \tag{3.2b}$$

We begin with the assumption that we have no current density, $\vec{J} = \vec{0}$. This term will be added back into for formulation when we discuss source terms in Section 3.5. Once we substitute $(0,0,E_z)^T$ and $(H_x,H_y,0)^T$ for $\vec{E}$ and $\vec{H}$, respectively, we have that

$$\mu\frac{\partial H_x}{\partial t} = -\frac{\partial E_z}{\partial y} \tag{3.3a}$$

$$\mu\frac{\partial H_y}{\partial t} = \frac{\partial E_z}{\partial x} \tag{3.3b}$$

$$\epsilon\frac{\partial E_z}{\partial t} = \frac{\partial H_y}{\partial x} - \frac{\partial H_x}{\partial y}. \tag{3.3c}$$

To work this into a discontinuous Galerkin formulation, we will need to write it in conservation form

$$\mathbf{K}\frac{\partial \vec{u}}{\partial t} + \vec{\nabla}\cdot\vec{f}(\vec{u}) = 0 \tag{3.4}$$

where $\vec{f}(\vec{u})$ is the flux function. We use bold font variables to represent matrix quantities. At this point we choose to define $\vec{u}(\vec{x},t)$ as

$$\vec{u} = \begin{pmatrix} H_x \\ H_y \\ E_z \end{pmatrix}. \tag{3.5}$$

The conservation form (3.4) can be expanded as

$$\mathbf{K}\frac{\partial \vec{u}}{\partial t} + \mathbf{F}_1\frac{\partial \vec{u}}{\partial x} + \mathbf{F}_2\frac{\partial \vec{u}}{\partial y} = 0 \tag{3.6}$$

since our flux function is a linear combination of $\vec{u}_x$ and $\vec{u}_y$. For $\vec{u}$ as defined by equation (3.5), we have

$$\mathbf{K} = \begin{pmatrix} \mu(\vec{x}) & 0 & 0 \\ 0 & \mu(\vec{x}) & 0 \\ 0 & 0 & \epsilon(\vec{x}) \end{pmatrix}, \mathbf{F}_1 = \begin{pmatrix} 0 & 0 & 0 \\ 0 & 0 & -1 \\ 0 & -1 & 0 \end{pmatrix}, \mathbf{F}_2 = \begin{pmatrix} 0 & 0 & 1 \\ 0 & 0 & 0 \\ 1 & 0 & 0 \end{pmatrix}. \tag{3.7}$$

Note that equation 3.4 is a slightly modified conservation form due the presence of the **K** matrix in front of the time derivative. This is to allow discontinuities in the ϵ and μ values. When these values are constant it would be easy to invert this matrix and merge it into the flux function.

We then introduce our test function $v(x)$, and split our domain into triangular elements Ω_j. We use a conformal mesh; however this requirement is not necessary for the DGM. The numerical domain formed by the mesh needs to converge to the physical domain as

$h \to 0$, but the cell sizes and shapes may be non-uniform (it is generally requested that all angles for any given element are larger than some fixed value in the range of 10 degrees). By multiplying by the test function, $v(x)$, and integrating over any mesh element we obtain

$$\int_{\Omega_j} v(x)\mathbf{K}\frac{\partial \vec{u}}{\partial t}\,\mathrm{d}V + \int_{\Omega_j} v(x)\vec{\nabla}\cdot\vec{f}(\vec{u})\,\mathrm{d}V = 0. \tag{3.8}$$

We use the vector calculus identity

$$\int_{\Omega_j} v\vec{\nabla}\cdot\vec{f}(\vec{u})\,\mathrm{d}V = \int_{\Omega_j} \vec{\nabla}\cdot(v\vec{f}) - \vec{f}\cdot\vec{\nabla}v\,\mathrm{d}V \tag{3.9}$$

along with the Divergence Theorem

$$\int_{\Omega_j} \vec{\nabla}\cdot(v\vec{f})\,\mathrm{d}V = \oint_{\partial\Omega_j} v\vec{f}\cdot\hat{n}\,\mathrm{d}s \tag{3.10}$$

to write

$$\int_{\Omega_j} v\vec{\nabla}\cdot\vec{f}(\vec{u})\,\mathrm{d}V = \oint_{\partial\Omega_j} v\vec{f}\cdot\hat{n}\,\mathrm{d}s - \int_{\Omega_j} \vec{f}\cdot\vec{\nabla}v\,\mathrm{d}V \tag{3.11}$$

where $\vec{n}$ represents the outward facing normal. Upon replacing $\vec{f}(\vec{u})$ with $(\mathbf{F}_1\vec{u}, \mathbf{F}_2\vec{u}, 0)^T$, we arrive at

$$\int_{\Omega_j} v\mathbf{K}\frac{\partial \vec{u}}{\partial t}\,\mathrm{d}V + \oint_{\partial\Omega_j} v(\mathbf{F}_1 n_x + \mathbf{F}_2 n_y)\vec{u}\,\mathrm{d}s - \int_{\Omega_j} (\mathbf{F}_1 v_x + \mathbf{F}_2 v_y)\vec{u}\,\mathrm{d}V = 0. \tag{3.12}$$

Equation (3.12) is the weak formulation of the TM Maxwell's equations which we will be discretizing.

The weak formulation can be generalized to three dimensions. However, this would be much more computationally intensive since instead of three equations there will be six (with the inclusion of E_x, E_y, and H_z) and the flux operator will include a third component.

Before we proceed, it is convenient to map each element, Ω_j, to the canonical element, Ω_0. In two dimensions with triangular meshes, we choose Ω_0 to be the triangle which connects vertices $(1,0), (0,1)$, and $(0,0)$. Furthermore, we will map the boundary integral to three one-dimensional integrals from $[-1,1]$, each integral representing a different edge of Ω_j.

Define the mappings

$$\begin{pmatrix} x \\ y \\ 1 \end{pmatrix} = \begin{pmatrix} x_1 & x_2 & x_3 \\ y_1 & y_2 & y_3 \\ 1 & 1 & 1 \end{pmatrix} \begin{pmatrix} 1-\eta-\zeta \\ \zeta \\ \eta \end{pmatrix} \tag{3.13}$$

and

$$\begin{pmatrix} x \\ y \end{pmatrix} = \begin{pmatrix} x_{a,q} & x_{b,q} \\ y_{a,q} & y_{b,q} \end{pmatrix} \begin{pmatrix} 0.5(1-\gamma_q) \\ 0.5(1+\gamma_q) \end{pmatrix} \tag{3.14}$$

where $x_{a,q} = x_q$ and $x_{b,q} = x_{q+1}$ except for $q = 3$, in which case $x_{b,3} = x_1$, with the same rules applying to the y values. This allows γ_q to represent the parameterization of the q^{th} edge of Ω_j from vertex $(x_{a,q}, y_{a,q})$ to $(x_{b,q}, y_{b,q})$

The Jacobian of the mapping defined by equation (3.13) is given by

$$\mathbf{J}_j = \frac{\partial(x,y)}{\partial(\zeta,\eta)} = \begin{pmatrix} x_\zeta & x_\eta \\ y_\zeta & y_\eta \end{pmatrix}. \tag{3.15}$$

Since the mapping is linear, $\mathbf{J}_j$ is a constant on each cell and is determined solely from the vertices of Ω_j. This Jacobian will have determinant

$$det(\mathbf{J_j}) = \frac{\text{Area}(\Omega_j)}{\text{Area}(\Omega_0)} = h_2 h_3 \sin(\theta_1), \tag{3.16}$$

where h_2 and h_3 are two side lengths of Ω_j, and θ_1 is the angle between these sides. Also, along any of the edges of the element

$$ds = \sqrt{\left(\frac{dx}{d\gamma_q}\right)^2 + \left(\frac{dy}{d\gamma_q}\right)^2} d\gamma_q$$

$$ds = \frac{\sqrt{(x_{b,q} - x_{a,q})^2 + (y_{b,q} - y_{a,q})^2}}{2} d\gamma_q \tag{3.17}$$

as a consequence of the change in arclength from the change in variables from s to γ_q.

We are now prepared to rewrite each of the three integrals from equation (3.12) in terms of our new variables. The first term in (3.12) becomes

$$\int_{\Omega_j} v(x,y)\mathbf{K}\frac{d\vec{u}}{dt}(x,y,t)\,dV = \int_{\Omega_0} \hat{v}(\zeta,\eta)\hat{\mathbf{K}}(\zeta,\eta)\frac{d\hat{\vec{u}}}{dt}(\zeta,\eta,t)det(\mathbf{J}_j)\,d\hat{V} \tag{3.18}$$

where the hat notation is used to indicate that at this step we have changed functions, namely $\hat{v}(\zeta,\eta) = v(x(\zeta,\eta), y(\zeta,\eta))$, and likewise for all other functions. The notation using hats will be dropped later for simplicity since all calculations are done on the canonical element, Ω_0.

The second integral can be rewritten as

$$\oint_{\partial\Omega_j} v(x,y)(\mathbf{F}_1 n_x + \mathbf{F}_2 n_y)\vec{u}(x,y,t)\,\mathrm{d}s$$
$$= \sum_{q=1}^{3}\int_{-1}^{1}\tilde{v}(\gamma_q)(\mathbf{F}_1 n_{x,q} + \mathbf{F}_2 n_{y,q})\tilde{\vec{u}}(\gamma,t)\frac{\sqrt{(x_{b,q}-x_{a,q})^2+(y_{b,q}-y_{a,q})^2}}{2}\,\mathrm{d}\gamma_q. \tag{3.19}$$

Here we use the notation that $\tilde{v}(\gamma_q) = v(x(\gamma_q), y(\gamma_q))$, and similar for $\tilde{\vec{u}}$. As with the hat notation this will not be continued and is just included for clarification of the parameterization. Also, we use $(n_{x,q}, n_{y,q})$ as the outward facing normal to the q^{th} edge of Ω_j.

Lastly, we also map the final integral in (3.12) to the canonical element,

$$\int_{\Omega_j}(\mathbf{F}_1 v_x + \mathbf{F}_2 v_y)\vec{u}(x,y,t)\,\mathrm{d}V = \int_{\Omega_0}(\mathbf{F}_1(\hat{v}_\zeta\zeta_x + \hat{v}_\eta\eta_x) + \mathbf{F}_2(\hat{v}_\zeta\zeta_y + \hat{v}_\eta\eta_y))\hat{\vec{u}}(\zeta,\eta,t)det(\mathbf{J}_j)\mathrm{d}\hat{V}. \tag{3.20}$$

We are now prepared to introduce our numerical approximations to the function $\vec{u}(\zeta,\eta,t)$ on the element Ω_j. The index j refers to which element we are working on, and index i refers to the basis function. On Ω_j we approximate $\vec{u}(\zeta,\eta,t)$ as

$$\vec{u}(\zeta,\eta,t) \approx \sum_{i=0}^{r}\begin{pmatrix} c_{ij}(t) \\ d_{ij}(t) \\ e_{ij}(t)\end{pmatrix}\psi_i(\zeta,\eta) \tag{3.21}$$

where $r+1$ is the number of basis functions we need to span all polynomials of degree less than or equal to p, the order of the desired basis. In two dimensions, the relationship is given by

$$r = \frac{(p+1)(p+2)}{2} - 1. \tag{3.22}$$

We also choose our test function to belong to the same finite dimensional space (a choice known as the Galerkin formulation)

$$v(\zeta,\eta) \approx \sum_{i=0}^{r} k_i\psi_i(\zeta,\eta). \tag{3.23}$$

It is easy to see that since each k_i can be chosen arbitrarily, we can bypass using this summation definition of our test function and instead say that the equations must hold for

$v(\zeta, \eta) = \psi_m(\zeta, \eta)$ for each $m = 0, 1, ..., r$. This simplification is available because each of the three integrals can be considered a linear operator on v (this result is not specific to Maxwell's equations).

So far we have not discussed our choice of basis functions, ψ. In the DGM, we define local basis functions, i.e., ψ_i is set to be zero for all values outside of Ω_0. By comparison, the same is not (and in fact cannot) be true of the basis used for finite element methods (since they require continuous basis functions). We will choose a basis which spans the set of all polynomials in (ζ, η) on Ω_0 up to degree p and will not require these functions to be zero along the boundary of the element. This choice of basis is what causes the DGM to produce discontinuous solutions between different cells, but the solutions remain continuous on each individual element. We will denote this set of basis functions $\mathbb{P}_p$.

When we substitute these new choices for $\vec{u}$ and v into (3.12), this allows us to rewrite the first integral as

$$\int_{\Omega_0} v(\zeta, \eta)\mathbf{K}\frac{d\vec{u}}{dt}(\zeta, \eta, t)det(\mathbf{J}_j)\, dV = \mathbf{K}det(\mathbf{J}_j)\sum_{i=0}^{r}\frac{d\vec{c}_i}{dt}\int_{\Omega_j}\psi_i\psi_m dV,\ \forall\psi_m \in \mathbb{P}_p \tag{3.24}$$

assuming that the $\mathbf{K}$ matrix is constant on Ω_j (which is the case if the electromagnetic coefficients do not change within a given element, but may change across elements). We also know that $det(\mathbf{J}_j)$ is constant for the mapping $\Omega_j \to \Omega_0$. Here we see that the increased flexibility on our basis functions is likely to be very rewarding since the DGM allows us to choose an orthogonal basis, a simplification not available to FEM.

The second integral requires the use of a Riemann solver (discussed in detail in Section 3.3). Since we will be using explicit time stepping, everything in this integral is known (besides how to choose the value of u when it is discontinuous, which is the task of the Riemann solver), we are able to evaluate this integral numerically for each ψ_m. Similarly, the values inside the third integral are known, so we can numerically integrate this integral as well.

This leads us to the system of three equations which must be true for each element,

$$\begin{aligned}
&\mathbf{K}det(\mathbf{J}_j)\sum_{i=0}^{r}\frac{d\vec{c}_i}{dt}\int_{\Omega_0}\psi_i\psi_m dV \\
&+\sum_{q=1}^{3}(\mathbf{F}_1 n_{x,q} + \mathbf{F}_2 n_{y,q})\frac{\sqrt{(x_{b,q}-x_{a,q})^2 + (y_{b,q}-y_{a,q})^2}}{2}\int_{-1}^{1}\tilde{\psi}_m(\gamma_q)\tilde{\vec{u}}(\gamma, t)\,\mathrm{d}\gamma_q \\
&- det(\mathbf{J}_j)\int_{\Omega_0}(\mathbf{F}_1(\frac{\partial\psi_m}{\partial\zeta}\frac{\partial\zeta}{\partial x} + \frac{\partial\psi_m}{\partial\eta}\frac{\partial\eta}{\partial x}) + \mathbf{F}_2(\frac{\partial\psi_m}{\partial\zeta}\frac{\partial\zeta}{\partial y} + \frac{\partial\psi_m}{\partial\eta}\frac{\partial\eta}{\partial y}))\hat{\vec{u}}(\zeta, \eta, t)\mathrm{d}V = 0,\ \forall\psi_m \in \mathbb{P}_p
\end{aligned} \tag{3.25}$$

here $q = 1, 2, 3$ corresponds to the three edges of each triangular element, $\vec{c}_i = (c_{ij}, d_{ij}, e_{ij})^T$, and $\vec{u}$ is also a three vector of the three unknowns. ψ_m can be any one of the chosen basis functions up to degree p.

Now, as is done with FEM, we define the mass matrix as the matrix operator in front of the $\frac{d\vec{c}}{dt}$ terms. Since this problem is linear, we could attempt to also define a stiffness matrix which would act on the $\vec{c}$ terms, however it does not provide much insight to do so in this application. Instead we will express the second and third integral components as a vector with r entries, one for each basis function substituted in for our test function, v. This formulation will be element-wise, so we will handle r equations at a time ($3r$ once we include the fact that $\vec{u}$ or equivalently $\vec{c}_{ij}$ is a three-vector). Alternatively, as is the case with FEM, the global system would have to handle $3r$ times the number of elements equations at a time.

Before writing equation (3.25) in a final form, we are free to choose our basis functions to simplify this equation. The most logical choice is to choose orthogonal basis functions; this will make our computations much simpler. Fortunately, order p orthogonal basis functions on the canonical right triangle are presented in [24]. These polynomials are defined as

$$\psi_i^k = P_{k-i}^{0,2i+1}(1-2\xi)(1-\xi)^i P_i(1-\frac{2\eta}{1-\xi}), \qquad k = 0, 1, \ldots, p, \qquad i = 0, 1, \ldots k. \tag{3.26}$$

where the superscripts on ψ indicate the polynomial degree, and the subscripts distinguish the different basis elements of a given degree. These orthogonal basis functions are formed by the product of Jacobi and Legendre polynomials. The Jacobi polynomials $P_n^{\alpha,\beta}(x)$ are orthogonal on [-1,1] with respect to the weight function $(1-x)^\alpha(1+x)^\beta$ in the standard L_2 norm as demonstrated in [1]

$$((1-x)^\alpha(1+x)^\beta P_n^{\alpha,\beta}, P_m^{\alpha,\beta}) = 0, \quad m \neq n. \tag{3.27}$$

Furthermore, the polynomials are normalized so that

$$P_n^{\alpha,\beta}(1) = \left(\begin{array}{c} n+\alpha \\ n \end{array} \right). \tag{3.28}$$

The Legendre polynomials, $P_n(x)$, are a subset of the Jacobi polynomials, formed by the choice $\alpha = 0$ and $\beta = 0$, that is to say $P_n(x) = P_n^{0,0}(x)$. The superscripts are typically dropped in the case of Legendre polynomials for convinience. All Jacobi polynomials also have the property that they will have n distinct roots on $(-1, 1)$. More thorough explanations of these orthogonal polynomials and their properties can be found in [39, 1].

With our basis functions chosen as

$$\{\psi_0^0, \psi_0^1, \psi_1^1, ..., \psi_p^p\}, \tag{3.29}$$

we proceed to solve (3.25). Let us define

$$\vec{c}_j = (c_{0j}, c_{1j}, ..., c_{rj}, d_{0j}, d_{1j}, ..., d_{rj}, e_{0j}, e_{1j}, ..., e_{rj})^T. \tag{3.30}$$

This results in the mass matrix on Ω_j

$$\mathbf{M}_j = \mathbf{K} \begin{pmatrix} \mu(x,y)\mathbf{A} & 0 & 0 \\ 0 & \mu(x,y)\mathbf{A} & 0 \\ 0 & 0 & \epsilon(x,y)\mathbf{A} \end{pmatrix} det(\mathbf{J}_j), \tag{3.31}$$

where the matrix $\mathbf{A}$ will be diagonal by the orthogonality of our chosen basis, with diagonal entries given by

$$A_{ii} = \int_{\Omega_0} \psi_i \psi_i dV. \tag{3.32}$$

We group the rest of the terms together into a single vector $\vec{l} = (\vec{l}^1, \vec{l}^2, \vec{l}^3)^T$ where:

$$\begin{aligned}(l_i^1, l_i^2, l_i^3)^T = &\sum_{q=1}^{3} (\mathbf{F}_1 n_{x,q} + \mathbf{F}_2 n_{y,q}) \frac{\sqrt{(x_{b,q} - x_{a,q})^2 + (y_{b,q} - y_{a,q})^2}}{2} \int_{-1}^{1} \tilde{\psi}_i(\gamma_q) \tilde{\vec{u}}(\gamma, t)\, \mathrm{d}\gamma_q \\ &- det(\mathbf{J}_j) \int_{\Omega_0} (\mathbf{F}_1 (\frac{\partial \psi_i}{\partial \zeta}\frac{\partial \zeta}{\partial x} + \frac{\partial \psi_i}{\partial \eta}\frac{\partial \eta}{\partial x}) + \mathbf{F}_2 (\frac{\partial \psi_i}{\partial \zeta}\frac{\partial \zeta}{\partial y} + \frac{\partial \psi_i}{\partial \eta}\frac{\partial \eta}{\partial y})) \vec{u}(\zeta, \eta, t) \mathrm{d}V.\end{aligned} \tag{3.33}$$

Now we are prepared to write this entire formulation as:

$$\mathbf{M}_j \frac{d\vec{c}}{dt} = \vec{l}. \tag{3.34}$$

Each component of $\vec{l}$ has contributions from two integrals, one over Ω_0 and another over its boundary, $\partial\Omega_0$. The boundary integrals contain a basis function times the numerical solution, each of which are represented by (up to) degree p polynomials. Therefore, the integration should be performed with sufficient accuracy to integrate polynomials of degree $2p$ exactly. This task is accomplished by using a numerical quadrature scheme of order $2p$. Having a numerical quadrature rule of this order is sufficient to prevent the evaluation of this integral from introducing its own errors into the solution. If the flux function was not linear, there would be $f(u)$ term(s) inside this integral, and we would need to improve the numerical quadrature to order $2p + 1$. Fortunately, the flux operator is linear in this problem. This linearity allows the use of precomputed coefficients if desired to quickly handle each of these integrals as a (precomputed) matrix times vector calculation. Numerical quadrature rules for use on triangular elements are discussed in [13].

Similarly, the volume integral present in each term of $\vec{l}$ will be computed using a numerical cubature. One could use a method employing precomputed coefficients if desired since this integral is also linear in $\vec{u}$. Also, since this integral features a derivative on the ψ function, the maximum degree of the integrand is reduced by one. Therefore, we require a numerical cubature to integrate this volume integral which is of order $2p-1$. The potential time saving idea of heavily precomputing these integrals is not applied because we prefer to maintain the flexibility to deal with nonlinearities, e.g. the case where μ and ϵ vary within a cell. This situation can be handled in the more general framework, but does require increasing the order of the numerical integration techniques depending on how $\mu(x, y)$ and $\epsilon(x, y)$ are approximated.

Once the vector $\vec{l}$ is determined, we can solve the ordinary differential equations (3.34) using a time stepping scheme. The usual choice is a Runge-Kutta scheme. Since the CFL condition tells us that the time step varies linearly with h, we desire a time stepping scheme of the same order of accuracy as the DGM method is in space. For a basis of order p, the DGM will feature an order of convergence of h^{p+1}, and a q step Runge-Kutta scheme will provide the order Δt^q for time step Δt. Therefore, we will need to use a Runge-Kutta scheme of order $p+1$ to attain the same order of convergence. This is the typically accepted strategy for pairing Runge Kutta with DGM and is applied in this work.

3.3 Riemann Problem

The Riemann problem addresses the issue of how to choose a value for $\vec{u}$ at a point where it is discontinuous. This arises between elements in the DGM since we allow $\vec{u}$ to be discontinuous here. Furthermore, the value of $\vec{u}$ is needed in the second integral in equation (3.25) along the boundaries between elements.

For our Riemann problem, we are able to find a good solution through upwinding. This solution would be exact in one dimension (however there are still errors from the time integration process) and will give good results in higher dimensions. For an in-depth explanation of the theory behind multi-dimensional Riemann solvers, we refer to [9] which includes the arguments of stability and convergence.

In one spatial dimension, our flux term appears in the discontinuous Galerkin formulation as

$$[f(u)]_{x_j}^{x_{j+1}} \tag{3.35}$$

after the one dimensional equivalent to steps (3.8)-(3.11). This can be thought of as a one dimensional boundary integral over the cell $[x_{j+1}, x_j]$. This leads us to the Rankine-Huogoniot condition

$$\lambda(u_2 - u_1) = f(u_2) - f(u_1) \tag{3.36}$$

which is obtained by cleverly applying a spatial integral to both sides the one-dimensional partial differential equation $\frac{\partial u}{\partial t} + \frac{\partial f(u)}{\partial x} = 0$ where $f(u) \approx \lambda u$ locally. Here u_2 and u_1 are the values of $u(x,t)$ on opposite sides of a discontinuity and λ is the speed with which the discontinuity propagates.

In two spatial dimensions, we see the term appearing as

$$\int_{\partial\Omega_j} \hat{n} \cdot \vec{f}(\vec{u}) dS. \tag{3.37}$$

This motivates the two dimensional Rankine-Huogoniot conditions

$$\lambda(u_2 - u_1) = (\hat{n} \cdot \vec{f}(u_2) - \hat{n} \cdot \vec{f}(u_1)). \tag{3.38}$$

To apply (3.38) to our Maxwell's equations, we must first include the **K** term. This is a straightforward extension and will appear beside the $\lambda(u_2 - u_1)$ terms, or equivalently can be inverted to the other side. However, we are careful since **K** may also be discontinuous along the boundaries between elements. We must also calculate what the λ's will be. This can be done either by an eigenvalue analysis of $\mathbf{K}^{-1}(\hat{n} \cdot \vec{f})$ or through knowledge of the physics of electromagnetic waves. Either way one comes to the conclusion that the three possible wave speeds are positive or negative c and zero (c represents the speed of light). If the two neighbouring cells consist of different media, the speed of light will be different on each side of the boundary.

The illustration (figure 3.1) and more details of this technique are included in [19]. In this figure, the vertical co-ordinate represents time and the initial condition is u_1 in cell 1 and u_2 in cell 2. Three discontinuities are formed from this Riemann problem, one moving in the positive direction, one in the negative direction, and one stationary. Each discontinuity separates two values for u, which introduces the need for two intermediate states labelled u^* and u^{**}. The Rankine-Huogoniot condition must hold across each of these lines and introduces the following set of three equations

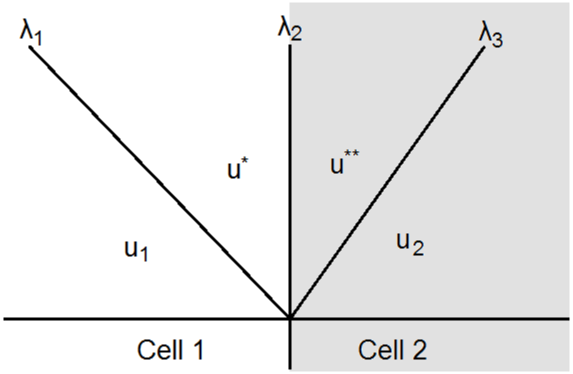

Figure 3.1: Sketch of the three wave speeds from TM Maxwell's equations. Three discontinuities are present at the interface described by the eigenvalues λ_1, λ_2, and λ_3 which define their propagation speeds.

$$c^{left}\mathbf{K}^{left}(\vec{u}^* - \vec{u}^{left}) + (n \cdot f(\vec{u}^*) - n \cdot f(\vec{u}^{left})) = 0 \tag{3.39a}$$
$$n \cdot f(\vec{u}^*) - n \cdot f(\vec{u}^{**}) = 0 \tag{3.39b}$$
$$-c^{right}\mathbf{K}^{right}(\vec{u}^{**} - \vec{u}^{right}) + (n \cdot f(\vec{u}^{**}) - n \cdot f(\vec{u}^{right})) = 0. \tag{3.39c}$$

These equations can be simplified using the following notation

$$\hat{n} \cdot f(\vec{u}) = \begin{pmatrix} 0 & 0 & n_y \\ 0 & 0 & -n_x \\ n_y & -n_x & 0 \end{pmatrix} \vec{u} = \mathbf{H}\vec{u}. \tag{3.40}$$

Therefore,

$$(c^{left}\mathbf{K}^{left} + \mathbf{H})(\vec{u}^* - \vec{u}^{left}) = 0 \tag{3.41a}$$
$$\mathbf{H}(\vec{u}^* - \vec{u}^{**}) = 0 \tag{3.41b}$$
$$(-c^{right}\mathbf{K}^{right} + \mathbf{H})(\vec{u}^{**} - \vec{u}^{right}) = 0. \tag{3.41c}$$

From this it follows that

$$\vec{u}^* - \vec{u}^{left} = \alpha\vec{r}_1 \tag{3.42a}$$
$$\vec{u}^{**} - \vec{u}^* = \beta\vec{r}_2 \tag{3.42b}$$
$$\vec{u}^{right} - \vec{u}^{**} = \gamma\vec{r}_3, \tag{3.42c}$$

where $\vec{r}_1$ is the eigenvector of $(c^{left}K^{left} + H)$ corresponding to the eigenvalue of zero, $\vec{r}_2$ is the eigenvector of H corresponding to eigenvalue zero, and $\vec{r}_3$ is the eigenvector of $(-c^{right}K^{right} + H)$ corresponding to eigenvalue zero. Given that $n_x^2 + n_y^2 = 1$ and μ, ϵ and c are all strictly greater than zero, these eigenvectors are given by

$$\vec{r}_1 = \begin{pmatrix} -n_y \\ n_x \\ c^{left}\mu^{left} \end{pmatrix}, \vec{r}_2 = \begin{pmatrix} n_x \\ n_y \\ 0 \end{pmatrix}, \vec{r}_3 = \begin{pmatrix} n_y \\ -n_x \\ c^{right}\mu^{right} \end{pmatrix}. \tag{3.43}$$

Now we can write

$$\vec{u}^{right} - \vec{u}^{left} = \gamma\vec{r}_3 + \beta\vec{r}_2 + \alpha\vec{r}_1 = \mathbf{R}\begin{pmatrix} \alpha \\ \beta \\ \gamma \end{pmatrix}. \tag{3.44}$$

We can solve the linear system (3.44) for α, β and γ. Solving for α, we obtain

$$\alpha = \begin{pmatrix} -n_y\mu^{right}c^{right} \\ n_x\mu^{right}c^{right} \\ 1 \end{pmatrix} \cdot \frac{(\vec{u}^{right} - \vec{u}^{left})}{\mu^{right}c^{right} + \mu^{left}c^{left}}. \tag{3.45}$$

Knowing α, we compute $\vec{u}^*$ as

$$\vec{u}^* = \vec{u}^{left} + \alpha\vec{r}_1. \tag{3.46}$$

Finally, we compute $\mathbf{K}^{-1}(\hat{n} \cdot \vec{f}(\vec{u}^*))$ as

$$\mathbf{K}^{-1}(\hat{n} \cdot \vec{f}(\vec{u}^*)) = (\mathbf{K}^{left})^{-1}(n_x\mathbf{F}_1 + n_y\mathbf{F}_2)\vec{u}^*. \tag{3.47}$$

Note that in this calculation we are on the left side of the interface, so the $\mathbf{K}$ matrix will use the left cell's coefficients. The value of $\mathbf{K}^{-1}(\hat{n} \cdot \vec{f}(\vec{u}^*))$ is the value we will use for the boundary integral in (3.12).

3.4 Numerical Boundary Conditions

Prescribed boundary conditions are incorporated into the DGM weakly, i.e., via the integral on the boundary of the numerical domain. If an element has one or more edges along the boundary of the domain, when we compute the boundary integral along these edges, the function is assumed to be discontinuous here. However, the value outside of the cell is unknown. We will proceed by handling this problem with the Riemann solver, but instead of sending the interior value from the cell and the value from the neighbouring cell, we use the interior value and a ghost state. Thus, we must choose the ghost state so that the resulting solution obtained through the Riemann solver satisfies the chosen boundary condition. Information which propagates into the ghost state is lost since the solution is not stored outside of the domain.

An important case is how we handle boundaries where we simply want the electromagnetic waves to pass out of the domain and not return. This type of boundary condition is desirable both for truly absorbing surfaces (blackbodies) and for truncated domains where we are not interested in what happens beyond this boundary. The second case is very important to allow us to speed up calculations since using a very large domain is extremely costly for DGM computations. Thus, using absorbing boundary conditions to truncate the domain is virtually a necessity. These boundary conditions are also known as radiative since they allow waves to leave the domain and return no new or reflected waves. Unfortunately, these conditions are not very simple to implement. While defining a ghost state of $\vec{u}^{ghost} = (0, 0, 0)^T$ might appear to provide an absorbing or radiating boundary condition, this method will fail to absorb any waves striking the boundary at oblique angles. However, this technique is extremely quick and, if the incidence is near-normal, accurate.

A more robust solution to model absorbing boundary conditions was developed in [4] where the theory of a perfectly matched layer (PML) was derived. The strategy is to replace the boundary with a layer of lossy material such that waves will enter the layer with no reflections back into the domain, and, through the lossy properties of the fictional layer, any information sent in will be lost and never return to the domain. As originally presented, applying the PML technique requires a small rework of Maxwell's equations, and is computationally expensive. But, the PML offers a perfect absorption making it an extremely valuable tool to time domain solvers in applications where extreme precision is mandatory. An alternative implementation presented in [33] does not require a reworking of Maxwell's equations within the layer, but does need the scheme to be able to handle anisotropic media. This approach has been shown to provide good results within the DGM framework [27].

Another useful boundary condition for modelling purposes is periodic and reflection conditions. Although these are different conditions, both suffice to maintain a plane wave on a finite domain which is otherwise impossible to do. A lot of electromagnetic theory is based on plane waves since plane waves produce parallel rays which is a good foundation for theoretical, geometrical optics. Furthermore, electromagnetic waves from distant sources are generally considered to act like plane waves up to a high degree of accuracy. Using either of these boundary conditions allows us to simulate plane waves without the large distance between the light source and region of interest. We choose to use perfectly reflecting boundary conditions for this task since the formulation does not require any knowledge of the geometry so it can be applied more easily to general boundaries. If the data on the interior of the boundary is given by $\vec{u} = (B_x, B_y, E_z)^T$, we use

$$\vec{u}^{ghost} = \begin{pmatrix} -B_x + 2n_x(B_x n_x + B_y n_y) \\ -B_y + 2n_y(B_x n_x + B_y n_y) \\ E_z \end{pmatrix}. \tag{3.48}$$

This statement implies the ghost state has the same electric field, and a magnetic field reflected over the normal to the interface.

Note that these boundary conditions result in no flux in the electric field through the boundary to conserve energy in the system (which needs to be true for a lossless reflection). If we consider extending equation (3.47), we can show we will get a flux vector of

$$\mathbf{K}^{-1}\hat{n} \cdot \vec{f}(\vec{u}^*) = \begin{pmatrix} \frac{n_y E_z^*}{\mu} \\ \frac{-n_x E_z^*}{\mu} \\ \frac{-n_x B_y^* + n_y B_x^*}{\epsilon} \end{pmatrix} \tag{3.49}$$

with B_x^*, B_y^* and E_z^* being the components of $\vec{u}^*$ given by (3.46). The last component can be expanded since with this specific choice of ghost cell value ($\vec{u}^{right}$) and equivalent values for μ, ϵ and c on both sides of the boundary, we will have

$$\vec{u}^{right} - \vec{u}^{left} = 2 * \begin{pmatrix} -B_x + n_x(B_x n_x + B_y n_y) \\ -B_y + n_y(B_x n_x + B_y n_y) \\ 0 \end{pmatrix} \tag{3.50}$$

which leads to

$$\alpha = n_y B_x - n_x B_y. \tag{3.51}$$

Thus,

$$B_x^* = B_x - n_y(n_y B_x - n_x B_y) \tag{3.52a}$$

$$B_y^* = B_y + n_x(n_y B_x - n_x B_y) \tag{3.52b}$$

by (3.46). So the electric field flux is

$$\frac{1}{\epsilon}(-n_x(B_x - n_y(n_y B_x - n_x B_y)) + n_y(B_y + n_x(n_y B_x - n_x B_y)) = 0 \tag{3.53}$$

(using $n_x^2 + n_y^2 = 1$). This means that our reflective boundary condition does not allow the electric field to pass through the boundary.

3.5 Initial Conditions and Source Terms

Maxwell's equations consist of four equations, however only two of these are modelled. The reason the other two are omitted is because they can be shown to be initial conditions of equations (1.2a) and (1.2c) [5]. Taking the divergence of Ampere's circuital law (1.2c) we get

$$\frac{\partial(\nabla \cdot \vec{D})}{\partial t} + \nabla \cdot \vec{J} = 0 \tag{3.54}$$

where we use the vector calculus identity $\nabla \cdot \nabla \times \vec{a} = 0$. We combine this with the conservation of charge which states that

$$\nabla \cdot \vec{J} = -\frac{\partial \rho}{\partial t} \tag{3.55}$$

to get to the re-expression of the law as

$$\frac{\partial}{\partial t}(\nabla \cdot \vec{D} - \rho) = 0. \tag{3.56}$$

This tells us that as long as Gauss' law (1.2b) is satisfied at the initial time, the time stepping scheme will preserve this relation (assuming the numerical errors are not too large to disrupt it). The same relation can be shown between Faraday's law (1.2a) and Gauss' law for magnetism (1.2d).

As a consequence of this, we need to ensure that the initial conditions satisfy (1.2b) and (1.2d). The simplest approach to doing this is to set initial conditions to zero everywhere and use the source to initialize the electromagnetic wave(s) we wish to observe.

If the equation includes source terms (denoted $\vec{s}(x, y, t)$), they appear in the original partial differential equation as

$$\mathbf{K}\frac{\partial \vec{u}}{\partial t} + \mathbf{F}_1\frac{\partial \vec{u}}{\partial x} + \mathbf{F}_2\frac{\partial \vec{u}}{\partial y} = \vec{s}(x, y, t). \tag{3.57}$$

After the introduction of test function and integration, this source term will add a new term to the right side of the formulation (3.34) given by

$$\int_{\Omega_j} \psi_m \vec{s}(x, y, t) dV. \tag{3.58}$$

These terms can be merged into the $\vec{l}$ term and evaluated by applying the same numerical cubature rule (for each ψ_m) as was done with the other integral over Ω_j. Note that as with the other terms in $\vec{l}$ this source contribution needs to be organized in three blocks of $r+1$ terms each, where $r+1$ represents the number of basis functions. Equation (3.34) now becomes

$$\mathbf{M}\vec{c} = \vec{l} + \begin{pmatrix} \int_{\Omega_j} \psi_0 s_1(x,y,t)dV \\ \vdots \\ \int_{\Omega_j} \psi_r s_1(x,y,t)dV \\ \int_{\Omega_j} \psi_0 s_2(x,y,t)dV \\ \vdots \\ \int_{\Omega_j} \psi_r s_2(x,y,t)dV \\ \int_{\Omega_j} \psi_0 s_3(x,y,t)dV \\ \vdots \\ \int_{\Omega_j} \psi_r s_3(x,y,t)dV \end{pmatrix}. \tag{3.59}$$

The source term is free to be anything; however, realistic simulations come from using an oscillating source since electromagnetic waves propagate through space as oscillations. This still leaves one with the freedom to choose where the disturbance(s) come from within the domain, the frequency and amplitude as well as whether the electric and/or magnetic field should be forced. In our simulations, we have found it to be most straight forward to use the forcing term to initialize the electric field only; since the magnetic fields will quickly adapt to try to form a wavefront propagating in every direction from the source. Also, if we recall the original Maxwell's equations, we see that the equation for $\frac{\partial \vec{E}}{\partial t}$ contains a source term ($\vec{J}$) which we chose to temporarily omit in Section 3.2. Adding a source into the electric field equation is effectively adding a current density into the physical problem modelled by Maxwell's equations. Alternatively, adding a source term to the magnetic fields is unrealistic since there does not exist a source term for magnetic field in Maxwell's equations. In our simulation, since we simulate the TM equations, the source term $\vec{J} = (0,0,J_z)^T$ will represent the current density which must be orthogonal to the domain; currents travelling within the domain do not fit in the TM framework because they induce a three dimensional electromagnetic response.

One way to initiate a plane wave is through making a source the entire height of the domain and a small width paired with reflective boundary conditions on the top and bottom walls of a square domain. A plane wave source like this is described in (4.1). Another practical simulation is to use a Gaussian beam, which is obtained by multiplying the previous source term by a Gaussian distribution in the vertical co-ordinate, as demonstrated in (4.13). The source term is easily flexible enough to allow this planar or Gaussian profile to be rotated to suit the problem.

One may choose to define $\vec{s}$ to be a persistent oscillating source, or one which emits only a single pulse. The first case will lead to steady state solutions, interference patterns and a representation of what happens in most realistic applications. In contrast, emitting a single pulse will create a data set which will trace the exact trajectory of the given wave and can be very illustrative when investigating wave focusing or creating visualizations. Using a single wave pulse can also be used to separate frequency dependent features from those independent of frequency by telling us if the observed features in the solutions are a consequence of a wave interfering with itself, or with other waves. In the numerical examples presented later, a variety of different source terms are applied to model the desired incident waves (equations (4.1),(4.2),(4.8),(4.11),(4.13)).

Simulations involving a single pulse can be initialized through either initial conditions or from a short-timed source term, whereas the persistent oscillator cannot be simulated from initial conditions alone. For this reason and to bypass any concerns of violating Gauss' law (1.2b) or Gauss' law for magnetism (1.2d) we find it easier to use a source term and keep the initial conditions fixed to zero throughout the domain.

A final, important, note with regard to the source term is that introducing oscillating source(s) or a fixed width pulse to the simulation determines the wavelength(s) present in the solution. The mesh needs to be able to properly resolve these wavelengths. Otherwise, the scheme will produce poor, under-resolved results and will generally be very dissipative. If the initial conditions were not zero they too would have this effect on the required mesh size.

3.6 Sensors and Data

When running simulations there are several outputs we may be interested in. Naturally, the unknowns of Maxwell's equations, the electric and magnetic fields, are informative. Also of interest is the intensity, given by the formula

$$I = |\frac{1}{\mu_0}\vec{E} \times \vec{B}| = \frac{1}{c\mu_0}|\vec{E}|^2 = \frac{n}{c_0\mu_0}|\vec{E}|^2 \tag{3.60}$$

where c_0 is the speed of light in vacuum, c the speed of light in the current medium, and n is the refractive index of the current medium. This makes use of two electromagnetic relationships: $|B| = c|E|$ and $c = nc_0$. What is even more important for many applications is the time averaged intensity field, which is collected at every time step and averaged as the simulation progresses in time. This time averaged intensity, frequently referred to simply as the intensity because of how rapidly electromagnetic simulations reach pseudo-steady state, is what is detected by most physical detectors including the human eye and even photographs (despite our tendency to think of them as capturing a single instant in time). Collecting the time averaged intensity data is important because it allows us to distinguish between interference patterns characteristic of the physical problem, and oscillations caused by the waves travelling through the system at that instant in time which are usually not detectable. When the Young's Double Slit experiment is simulated (Section 4.2), it is the time averaged intensity that gives us the meaningful result of the characteristic fringe pattern we hope to see, while the instantaneous distributions shows us the expected pattern convoluted with an interference pattern oscillating at the frequency of the waves in the system.

The time averaged intensity data will change rapidly during the transient state of the simulation, which is physically very short. Once the pseudo-steady state is reached, the intensity distribution will consist of standing waves between zero and some maximum value. So, the time averaged intensity will tend towards a steady state distribution of average intensity. Since the time average includes all time steps, the transient information will become less influential over time and the time averaged intensity distribution will tend towards its true steady state. It is also useful to use a source which is only active for a finite amount of time, and collect data until all the information has left the domain. This practice will ensure the averaging does not collect an uneven amount of waves in different parts of the domain. If this is not done, it causes an effect which makes the earlier parts of the domain appear to have more average intensity in them than they should since they have seen more waves pass by.

One last output we can examine is the velocity. Electromagnetic velocity is defined by the cross product of the electric and magnetic fields. Knowing the velocity distribution can give useful insight into features like how diffraction may be influencing the system and what the angles of incidence are along a surface.

The data available from running a time domain simulation exceeds that from a frequency domain simulation since we are able to run absolutely any type of source, even a single pulse. Furthermore, we may collect data before the standing wave pattern is established to gain more insight into the phenomena at work.

Chapter 4

Numerical Examples

In this section we present a number of examples demonstrating some simulations for which the DGM is applicable. We successfully model problems which may be challenging for other techniques for a variety of reasons including the necessary inclusion of diffraction and interference, as well as implementing boundaries between different media and resolving focal points which may be tough to capture.

4.1 Coffee Cup Caustic

The first simulation we perform with the DGM is to model the caustic formed when electromagnetic waves strike a circular mirror in the two dimensional plane. This caustic is often seen in the bottom of a coffee cup where light waves from a distant source reflect to create a characteristic pattern as seen in figure 4.1. Our simulation will feature plane waves (like those coming from a distant light source) interacting with a circular mirror to produce an intensity distribution known as a caustic.

A caustic is defined as the envelope of reflected or refracted rays [18]. It is the region where the non-incident rays are interacting with each other to make a focusing pattern. A caustic is typically a generalization of a focal point which arises from including the full set of rays, instead of just the idealized rays. This leads to the formation of a high intensity region (instead of a single point). Caustics and focal points are problematic for analysis with simpler schemes like ray-tracing since the geometry can lead the scheme to arrive at infinite values for intensity unless specifically handled, usually by incorporating diffraction into the scheme [36].

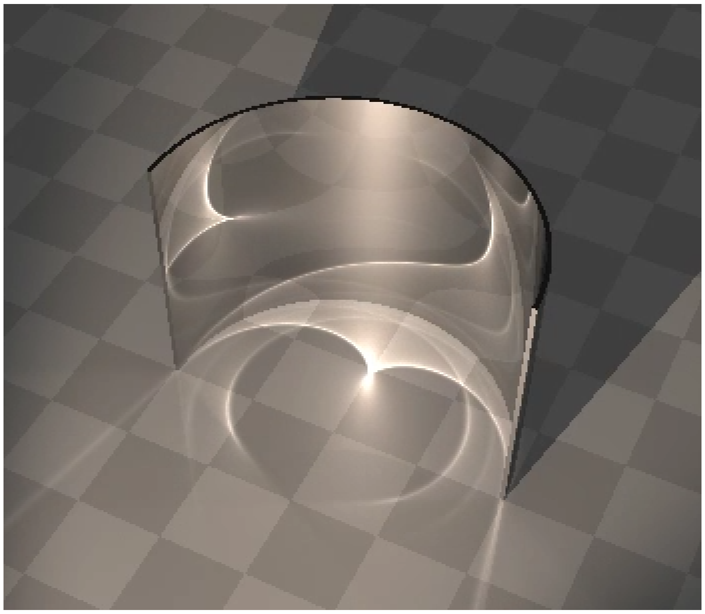

Figure 4.1: The coffee cup caustic simulated using POV-Ray, a 3D geometrical optics software package

The exact expectations for this simulation are much more elusive than what a simple application of geometric theory may suggest. A well known, and often misunderstood, result from geometrical optics is that a spherical (or circular) mirror has a focal point at half its radius, i.e., $0.5R$. This result is a simplification for a number of reasons. The $0.5R$ focal point is obtained only in the paraxial ray approximation, i.e., only considering rays which strike extremely near the centre of the mirror. When we include non-paraxial rays, the system experiences spherical aberration: the rays farther off the axis miss the theoretical focal point and spread the concentrated intensity into other areas which will define the caustic. Simple ray-tracing suggests the distribution of the reflected light rays should produce a caustic defined by a nephroid [35], with a lot of rays focusing near the $0.5R$ point, and the more aberrated rays forming the rest of the shape as shown in figure 4.2. This ray-tracing simulation can be performed by POV-Ray as demonstrated in figure 4.1. In this figure, we direct a very distant light source at a slightly elevated angle toward half of a cylindrical reflector. The intensity distribution is then displayed on the floor beneath the mirror. This simulation is very similar to the two dimensional simulation we will perform with the DGM since the elevated angle is small (and in fact is only necessary to project the image onto the floor below), and a distant light source becomes equivalent to planar incident waves as the distance between source and mirror approaches infinity. However, the ray-tracing simulation does not properly model all of the features. Ray-tracing does not account for interference within the reflected rays as well as interference between reflected and incident rays, unless care is taken to include these processes. Furthermore, there is also diffraction which we would be neglecting in the simple ray-tracing model.

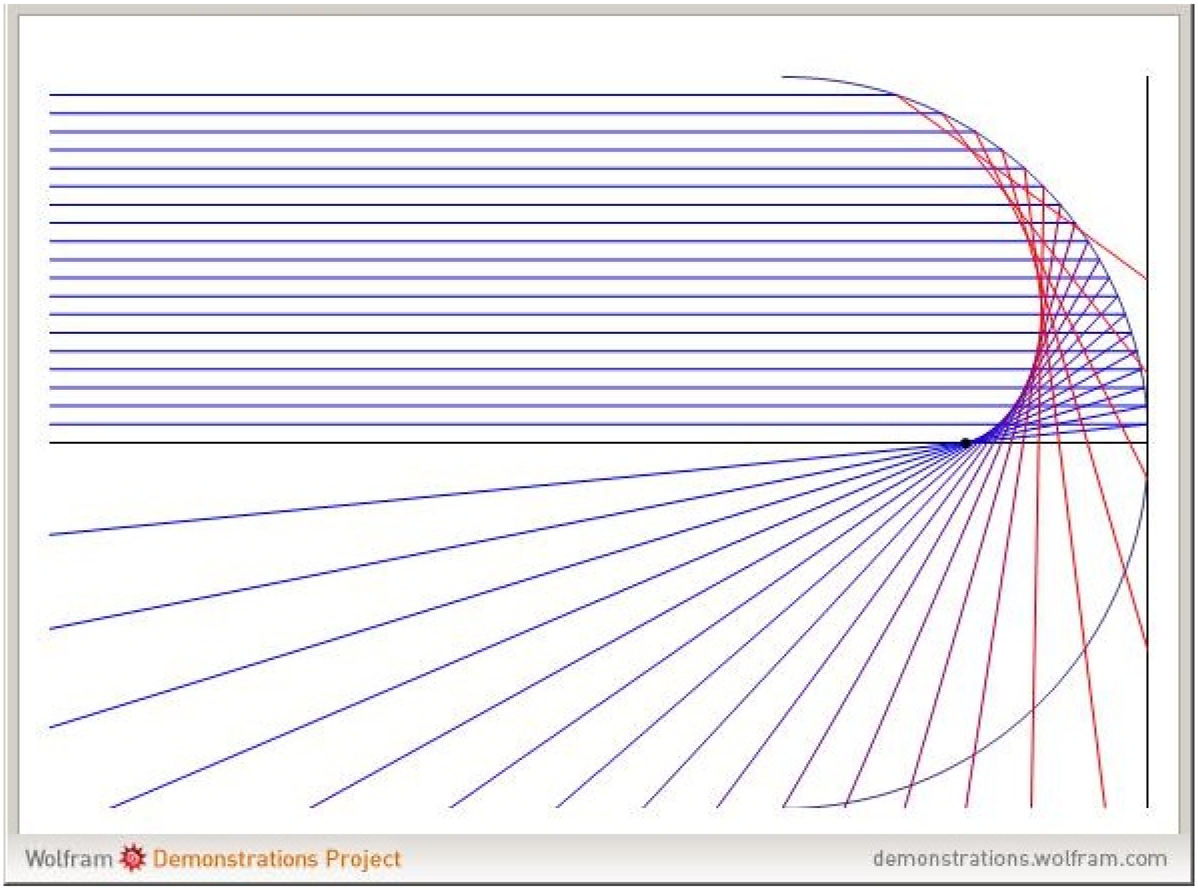

Figure 4.2: A demonstration of paraxial rays (which are blue upon reflection) which intersect at the expected focal point, and non-paraxial rays (which are red upon reflection) which cause spherical aberrations.

Experiments performed with high frequency electromagnetic waves confirm that a caustic is formed in this experiment, and that its shape is approximated by the nephroid shape predicted via geometrical optics (an approximation which is expected to be valid for high frequency waves). As such, our simulation will need to handle the formation of this caustic and the rapid changes in the amplitude of the electric and magnetic fields it results in. Many schemes will struggle here as the steep gradients can cause major hazards for numerical solvers. The discontinuous Galerkin method offers a technique easily capable of handling this near-discontinuous distribution of intensity. As a consequence of the discretization of Maxwell's equations, the DGM and other time domain schemes can incorporate interference and diffraction into the solutions naturally.

Also, since we know we have results for convergence and stability for discontinuous Galerkin method in two dimensions (these results are shown in [9]), we can get a good estimate on the accuracy of numerical solutions by comparing them to higher order or higher resolution simulations.

To begin, we use the mesh pictured in figure 4.3 and simulate an oscillating source of plane waves with a given frequency. We compare the time averaged intensities for various levels of refinement and polynomial bases of varying order on each cell. We compare the maximum intensity and location of the peak of the caustic (where this maximum is achieved) of the different simulations to the highest resolution case (third order basis and a mesh obtained by refining the original 9193 element mesh twice).

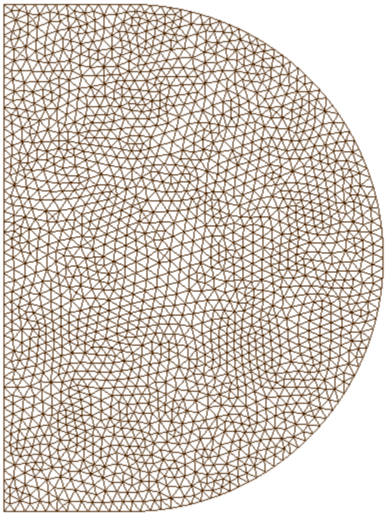

Figure 4.3: A 9193 element mesh used to simulate plane waves striking a circular mirror

In this simulation we are interested in a mirror or reflective circular surface with diameter of approximately 10cm. The mesh created features a circular mirror of diameter 2 dimensionless units; so we scale our problem to make 1 dimensionless unit represent 5cm. We create an oscillating source which induces an electric field of planar sine waves. The frequency of which will be equivalent to a 30GHz source after accounting for the scaling. This frequency represents a microwave (with 1cm wavelength) and falls into the classification of terahertz radiation. This source term is given by

$$\vec{s}(x,y,t) = \begin{cases} (0,0,\sin(20\pi t))^T & \text{if } x \in (-0.5,-0.45) \\ \vec{0} & \text{otherwise.} \end{cases} \tag{4.1}$$

This source term is activated in a narrow region defined by $x \in (-0.5, -0.45)$ with the centre of the circular mirror at the origin. Using the mesh in figure 4.3 we define the curved, top, and bottom boundaries to be perfectly reflecting. The curved boundary simulates the mirror; the top and the bottom are reflective to preserve the planar incident wave. The left boundary is simply radiative, allowing the reflected waves to leave the system. We allow the source to run for a long time (40 periods) before setting it to zero to terminate any more forcing. We capture the final values for the (time) averaged intensity once all the waves have left the domain as was discussed in Section 3.6. Allowing many wavelengths to traverse the system allows the interference effects in the steady state to be much more pronounced than any transient effects.

Data is collected for three levels of refinement in both the order of the basis (p-refinement) and cell size (h-refinement). Starting with the mesh pictured in figure 4.3 ($h = h_1$), we refine cells by splitting each triangle into four ($h = h_2 \approx \frac{h_1}{2}$) then again into sixteen ($h = h_3 \approx \frac{h_1}{4}$). The meshes are created and refined in GMSH. This software intelligently refines triangular elements so that when a triangle is split into four smaller ones, the smaller ones better adapt to the physical boundary wherever possible to avoid converging to an incorrect result from an incorrect numerical boundary (see figure 4.4). We also run this simulation using three different sets of polynomials basis (in x,y) on each element. In the first case ($p = 1$) we use linear polynomials, next ($p = 2$) we use up to and including quadratic polynomials, and lastly ($p = 3$) cubic polynomials to give a third order basis. The time averaged intensity fields for each simulation are shown in figure 4.5. These results show the expected pattern with an interference pattern caused by the wavelength of the EM waves. We also see that the three lowest resolutions ($h = h_1$, $p = 1, 2$ and $h = h_2$, $p = 1$) show significant diffusion resulting in an inaccurate simulation. In the bottom right is the most accurate simulation, which shows good agreement with the neighbouring simulations suggesting, through the properties of convergence, that this numerical solution has achieved a high level of accuracy.

A more detailed analysis is presented in tables 4.1, 4.2 and 4.3. We determine the position of the true focal point by the prediction of the ($h = h_3$, $p = 3$) simulation and

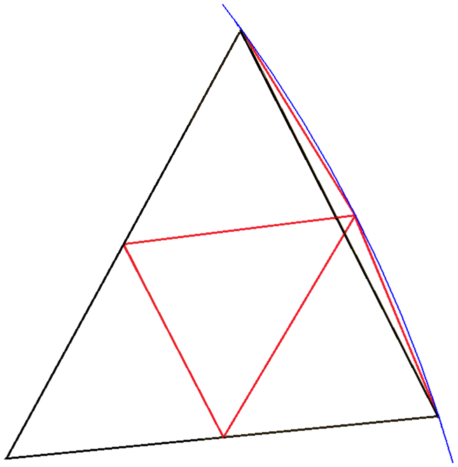

Figure 4.4: A large cell (in black) is refined to make four smaller cells (in red). The smaller cells better adapt to the physical boundary so the numerical domain converges to the physical one.

		p refinement		
		1	2	3
	1	0.005*	5.2569	13.4707
href	2	1.6333**	14.1101	15.0793
	3	11.2750	15.0027	15.1481

Table 4.1: Maximum value of time averaged intensity obtained in at the focal point.

		p refinement		
		1	2	3
	1	N/A*	(0.552,0.005)	(0.544,0.002)
href	2	(0.539,0)**	(0.547,0.002)	(0.548,-0.0006)
	3	(0.547,0.002)	(0.547,-0.0006)	(0.547,0.0006)

Table 4.2: Location of the focal point from the circular mirror.

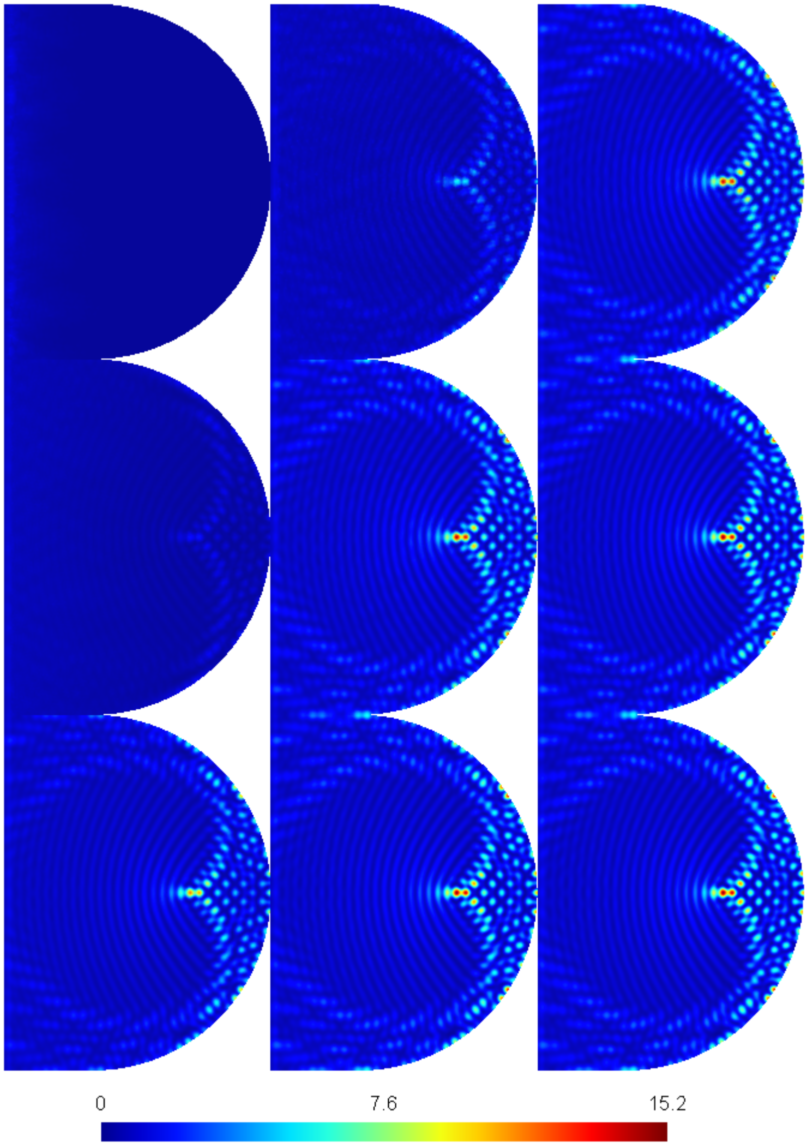

Figure 4.5: Time averaged intensity from a circular mirror obtained using different combinations of *hp*-refinement. Top row is the unrefined mesh (figure 4.3), each row below is one further level of h-refinement. Leftmost column are simulations with $p = 1$, middle column uses $p = 2$ and on the right, $p = 3$.

		p refinement		
		1	2	3
	1	0.04	0.17	0.59
href	2	0.20	1	3.63
	3	1.25	6.29	25

Table 4.3: Relative time taken for simulations compared to $h = h_2$, $p = 2$ case.

measure the peak value in this neighbourhood for all nine simulations in table 4.1. The results are very good for the three best resolutions (bottom right of the tables), and quite poor for the three least resolved simulations (top left of the tables). In the two worst cases, when $p = 1, h = h_1$ or $p = 1, h = h_2$, the diffusion very negatively affected the maximum value obtained at the peak. Here, when $h = h_1$ (as labelled by (*)) the propagating wave decayed enough that the maximum value was almost completely lost, and when $h = h_2$ (as labelled by (**)) the diffusion caused the peak occurring next to the true focal point to have a larger intensity, however this value was not used. A congruent analysis in table 4.2 looks at the location of the focal point with the different levels and methods of resolution. Again the same two cases experience very clear problems, in (*) the exact location is not even clear, and in (**) there is an alternative peak which shows a larger max value (a consequence of the diffusion in this simulation). The location of the focal point appears to be much more resistant to error, since all cases besides the two worst provide quite good approximations of the location. As expected, the maximum value does not appear at the paraxial ray approximation value of (0.5,0) for any simulations. Instead, this analysis shows the focal point at approximately (0.547,0), which is closer to the mirror than the incomplete theory suggests. This finding is supported by the presence of spherical aberration. In figure 4.2, we clearly see that the rays not accounted for in the paraxial approximation will cross the x-axis between the focal point and the mirror. This behavior will cause the maximum intensity to be observed somewhere between the paraxial ray prediction, $(0.5, 0)$, and the mirror's x-intercept, $(1, 0)$, as we have found.

When we detect electromagnetic fields in everyday experience, it is the time averaged intensity that we are able to see or capture. Since EM waves travel and oscillate so incredibly fast, the standing wave pattern, which is formed almost instantly, is witnessed as a time average. However, when we see these patterns with visible light, we view the caustic as a solid nephroid shape, not a series of peaks forming a nephroid. In reality, the speckle pattern is present even within visible light, however the distance between peaks is so tiny that it is not detectable, and we are left with the crisp nephroid shape a physical experiment appears to produce. In figure 4.6, we have repeated the same simulation except increased the frequency of the source (and increased the resolution to maintain a good degree of accuracy). In this time averaged intensity image, we still have the speckle pattern, however the pattern has become finer and closer to what happens within the visible light range.

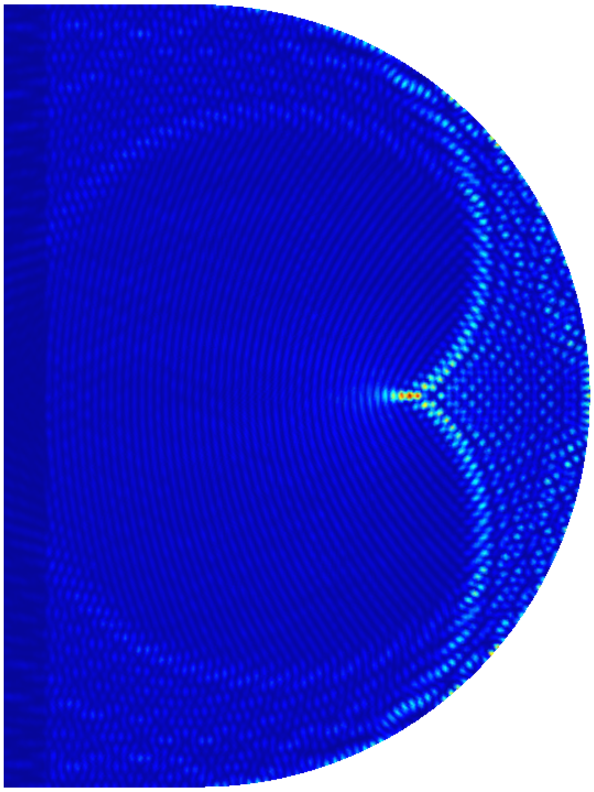

Figure 4.6: The time averaged intensity from the simulation of a high frequency, planar source.

It is also of interest that, because of the high degree of flexibility of the DGM, we may simulate other experiments which may give us information about specific properties of the setup. For instance, we may simulate a single pulse travelling through the domain. This simulation reveals which features are from interference from the same planar wavefront and which features are the results of separate wavefronts interacting. The latter effect will produce frequency dependent results, unlike the effects of a wave interfering with itself. This experiment also lets us investigate more clearly the presence of diffraction, and just how much of each wavefront ends up at the focal point. Although diffraction and interference are present in the simulation with an oscillating source, they are very difficult to isolate and quantify without this sort of analysis. Furthermore, since the speckle pattern that is present in the oscillating source simulations is a frequency dependent effect, it will not be present in the simulation of a single pulse traversing the domain. As such, the time averaged intensity field from this simulation looks more like what we see when this experiment is performed with visible light. This is no coincidence; simulating only a single pulse neglects the interference between different wavefronts. Although different wavefronts of visible light do interact, they are so closely packed together that the interference is not visible unless the experiment is intentionally set up to detect interference effects as is the case in Young's double slit experiments in Section 4.2.

The single pulse simulation is run in the same way the same as the oscillating case; however, the source term is only allowed to operate for half of one period (instead of for 40 full oscillations as was done before). For this simulation, we use the $h = h_2$ mesh and a second order basis on each cell ($p = 2$). In figures 4.8 and 4.9 we see this single plane wave interacting with the circular mirror. This simulation allows us to very cleanly access how each wave behaves in the system and how intense the focusing behavior is at specific moments in time. We also present the time averaged intensity from this simulation in figure 4.7 which, as predicted, closely resembles the distribution seen in physical experiments.

We expect the focal points in the two simulations (oscillating source and single pulse) to differ by less than one wavelength. This is a consequence of the interference pattern the wavelength may cause on the numerical (and physical) solutions when the source is a continuous oscillator. This is another reason why ray tracing is viable for ultra small wavelengths, but loses its usefulness for larger wavelengths. In the simulation shown in figure 4.7, the focal point appears at (0.576,0) which is roughly one third of a wavelength different from the focal point in the oscillating case.

As expected, our solution always improves with an increase in order of the basis functions used on each element (p-refinement) and with an increase in number of cells used to cover the domain (h-refinement). Furthermore, the data shows that for this simulation one step of p-refinement offers a larger increase in accuracy for a smaller cost in time than one level of h-refinement. This is a common result for the DGM that is a consequence of the error bound of order (approximately) h^{p+1} as mentioned in Section 2.1. Also, for this scheme the increase in time step size for one level of p-refinement is typically slightly less than one level of h-refinement, which contributes to a faster simulation. This behavior, where p-refinement is preferable to h-refinement, is seen in other applications of the DGM such as fluid flow around a cylinder as presented in [25]. As expected in these simulations we found that using a low order basis and large cells results in detectable diffusion; this

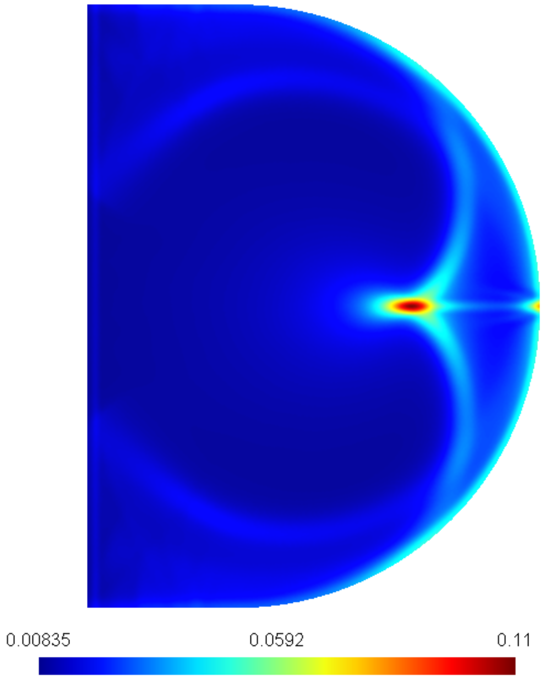

Figure 4.7: The time averaged intensity from the simulation ($h = h_2$, $p = 2$) of a single pulse propagating through the domain.

results in noticeable errors in the intensity at the focal point. However, the influence on the location of the focal point is much less pronounced than the effect of diffusion since even when the resolution was quite low and a large amount of diffusion was present the peak location varied very little from the most accurate result. As such, we can say that for this simulation the primary concern is to obtain a high enough degree of resolution through *hp*-refinement that the wave does not decay as it propagates. If this requirement is fulfilled, the simulation appears to be very reliable. Even under close investigation no undesired oscillations could be found in this simulation in the region of the focal point or elsewhere in the domain, indicating the DGM is a good technique for handling the steep gradients present in this numerical solution.

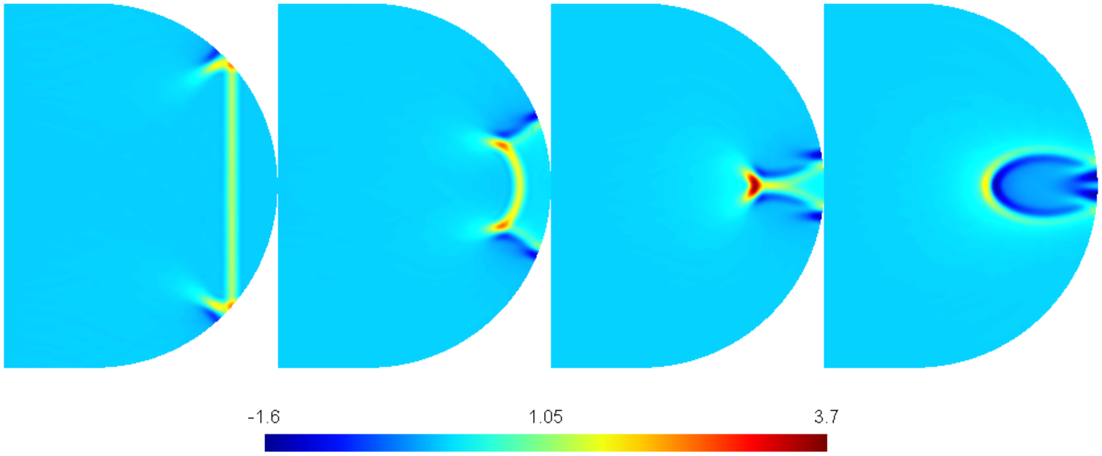

Figure 4.8: The electric field from the planar pulse at 4 different time steps increasing in time from left to right.

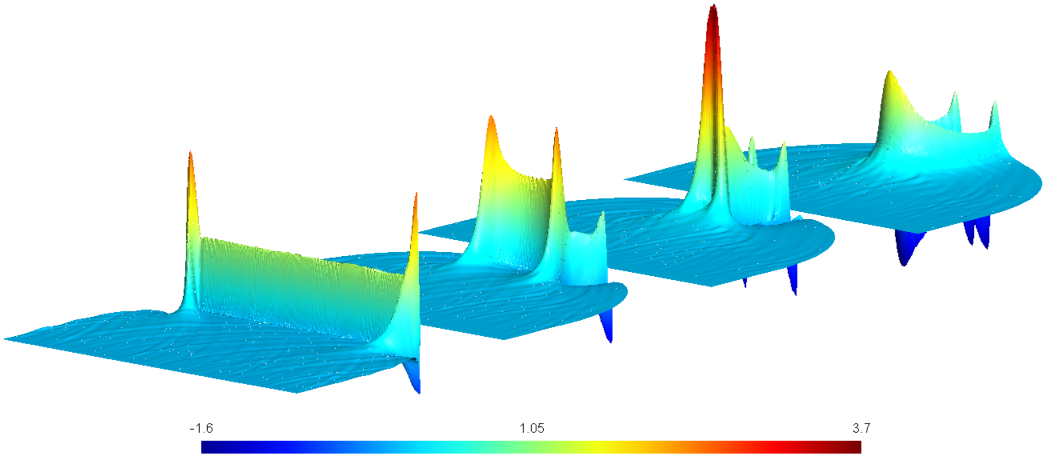

Figure 4.9: Three dimensional plots of the data in figure 4.8.

4.2 Young's Double Slit Experiment

Young's experiment is a physical experiment which illustrates the wave-particle duality of light and other electromagnetic waves. In this classical experiment, a coherent light source is aimed at an obstacle which has two narrow slits to allow light to pass through. Because of the diffraction that occurs, the slits act like two in-phase point sources of light. As a result, the wave nature of light causes light from the two different slits to interfere in a predictable pattern that cannot be explained using the theory that views light as particles. This pattern is observed as an alternating sequence of light and dark fringes on a screen placed anywhere behind the obstacle containing the slits. If the screen is a detector, the light is always received in discrete quantities which correspond to the energy from individual photons or "particles" of light, which illustrates the particle-like properties of electromagnetic waves. The aim of simulating this experiment is to demonstrate that, through the use of Maxwell's equations, we automatically simulate the wave properties such as interference and diffraction. Furthermore, since the experiment is well understood, we are able to compare the numerical solution to the physical theory.

Although the physical results of this particular experiment can be well approximated through ray-tracing by assuming the slits act as point sources, in general, implementing ray-tracing schemes with diffraction included can be troublesome. This is particularly true if the diffraction cannot be modelled to be localized around specific regions like corners or apertures. Schemes like FDTD, where the wave speed might not be accurately approximated in all directions, may also be unreliable for an application such as this since anisotropic errors would distort the interference pattern. Being able to accurately model this application with no special precautions demonstrates the durability of the DGM. This will allow us to generalize the simulation to accurately model less ideal geometric arrangements or wider slits with no extra effort. When the slits are narrow (relative to the wavelength) the diffraction at these apertures is so intense that the point source approximation is very accurate. However, if the slits are wide compared to the wavelength, the wave profiles leaving the slits will be poorly approximated by a point source since the diffraction is not strong enough to bend the wave into a full spherical wave. In this simulation we will use a slit width on the order of one wavelength. In this range the point source approximation is valid so we will be able to make meaningful comparisons.

Our simulation is done on the 26774 element mesh shown in figure 4.10. We initialize a plane wave source in the left part of the domain. The source oscillates to produce waves of wavelength $\lambda = 0.121$ in the scaled dimensions. The width of the source is 0.05, and it begins 0.45 units before the aperture (which is located at $x = 0$). The exact source function is given by

$$\vec{s}(x, y, t) = \begin{cases} (0, 0, \cos(\frac{2\pi t}{0.121}))^T & \text{if } x \in (-0.5, -0.45) \\ \vec{0} & \text{otherwise.} \end{cases} \tag{4.2}$$

The width of each of the two slits is $a = 0.12$, and the distance between slits (measured centre to centre) is $d = 0.68$. Along the line $x = 2.4$ we measure the electric field, in order to detect the light and dark fringes observed in the experiment. The simulation is performed using a third order basis on each element. For a chosen instant in time, sufficiently large so that any transient effects have passed, we collect the images of electric and intensity fields shown in figure 4.11. In both images we see the radiation leaving the right side of the aperture in a nearly spherical wave shape as expected for this slit width. We also see the patterns of constructive and destructive interference characteristic of this experiment.

As before, the data collected and observed in the physical experiment is not instantaneous distributions, but instead the time averaged pattern. In figure 4.12, we look at the average intensity in the domain over time. On the left of this figure is a surface plot, rotated to display the distribution a detector at the right boundary of the domain would record. We compare the data at our imaginary screen at $x = 2.4$ to what different theories predict should be observed. We begin by collecting the intensity along $x = 2.4$ at many different instants in time, taking care to wait long enough so that any transient effects have passed and the standing wave pattern has been established. In figure 4.13 we plot three of these distributions of intensity data (top), comparing height along the line $x = 2.4$ (on the horizontal axis) versus intensity (on the vertical axis). We then record the maximum value for each point on this line over a large number of time steps, which represents the amplitude of the oscillation at this point in the standing wave. The time averaged intensity at a given point will be half of the maximum intensity at that point since the intensity oscillates between zero and its maximum. For consistency, we also repeated the sampling process by taking the average over all time steps and found that the two approaches yielded similar results. However, the second method required extreme care not to introduce bias which occurs if the average is taken over a period of time which does not represent an integer number of oscillations in the standing wave pattern. The lower half of figure 4.13 shows the amplitude of the standing waves of intensity obtained with DGM at $x = 2.4$, it is this data set we will compare to theoretical results.

There are several theoretical results that can be used to describe the distribution resulting from the double slit experiment. One theory commonly used to approximate this experiment is the Fraunhofer diffraction theory. This theory applies when

$$\frac{(0.5d)^2}{\lambda} << R \tag{4.3}$$

or, equivalently, the Fresnel number, defined by $F = \frac{r^2}{R\lambda}$, where r is the characteristic radius of the aperture, is much smaller than 1. In our simulation $F = 0.4$, suggesting that the Fraunhofer approximation should be applied carefully.

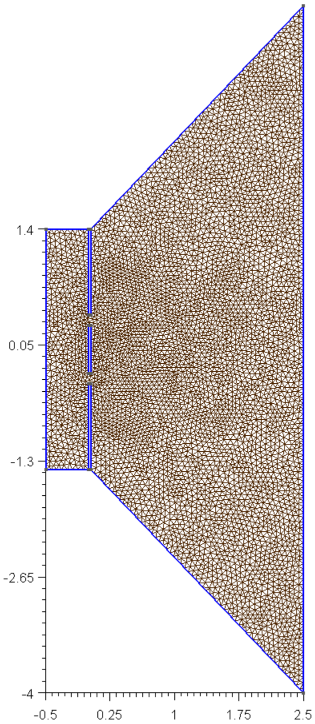

Figure 4.10: Mesh for simulating Young's double slit experiment

There are two predictions from the Fraunhofer diffraction theory, the first is the simplified version

$$I(y) = I_{Max}\left(\cos(\frac{dky}{2R})\text{sinc}(\frac{aky}{2R})\right)^2. \tag{4.4}$$

Here, d is the slit separation, a the slit width, R the perpendicular distance from slits to screen, y the variable describing the vertical location on the screen with $y = 0$ located directly between the two slits, and k the wavenumber defined by wavelength, λ, as $k = \frac{2\pi}{\lambda}$. This result comes from the linearization of Fraunhofer diffraction theory which assumes the angle (θ) from the centre between the two slits to the point (R, y) on the screen is well approximated by $\frac{y}{R}$ or, equivalently, θ is small. This approximation is only valid for small values of y. In figure 4.14, we compare the expectation from this linear Fraunhofer diffraction theory to the numerical results we obtained.

If we remove this last assumption on θ, we get the Fraunhofer diffraction theory solution

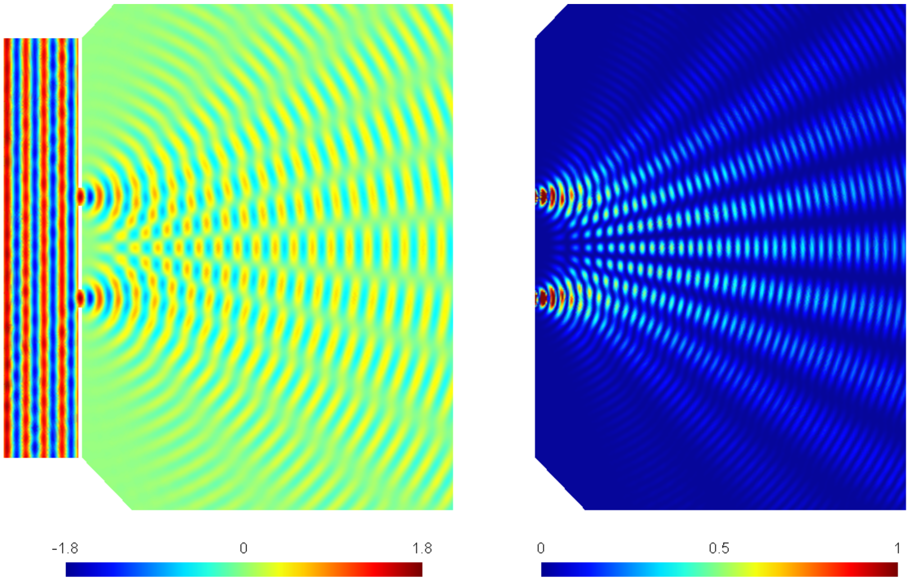

Figure 4.11: On the left, the electric field at one instant in time. On the right, the intensity distribution through the slits at that same instant.

of

$$I(\theta) = I_{Max}\left(\cos(0.5k\theta d)\mathrm{sinc}(0.5k\theta a)\right)^2 \tag{4.5}$$

this solution is are compared to our numerical results in figure 4.15. We see that the solutions from (4.4), (4.5) and the numerics match up very well for small values of y, but they disagree as y gets large. As expected, this effect is more pronounced in the solution given by the linearized theory; which is understood to lose accuracy as y gets larger. However, even in the general Fraunhofer diffraction theory, the DGM results deviate from predictions for $y \geq 1$. This could be a consequence of the Fraunhofer theory not being too reliable for the specifications in this problem.

Fortunately, another theoretical measure for this problem is to use geometrical ray optics to determine where the local maxima (usually called light fringes in optics) are expected to be located. Recalling that the approximation of the slits as point sources is reasonable if the slit width is on the order of, or smaller than, one wavelength, we are able apply this to approximate some features of this simulation through geometrical optics. Interestingly, since spherical wavefronts are perfectly simulated by geometrical optics, simulating two point sources and calculating the distribution along the screen can be

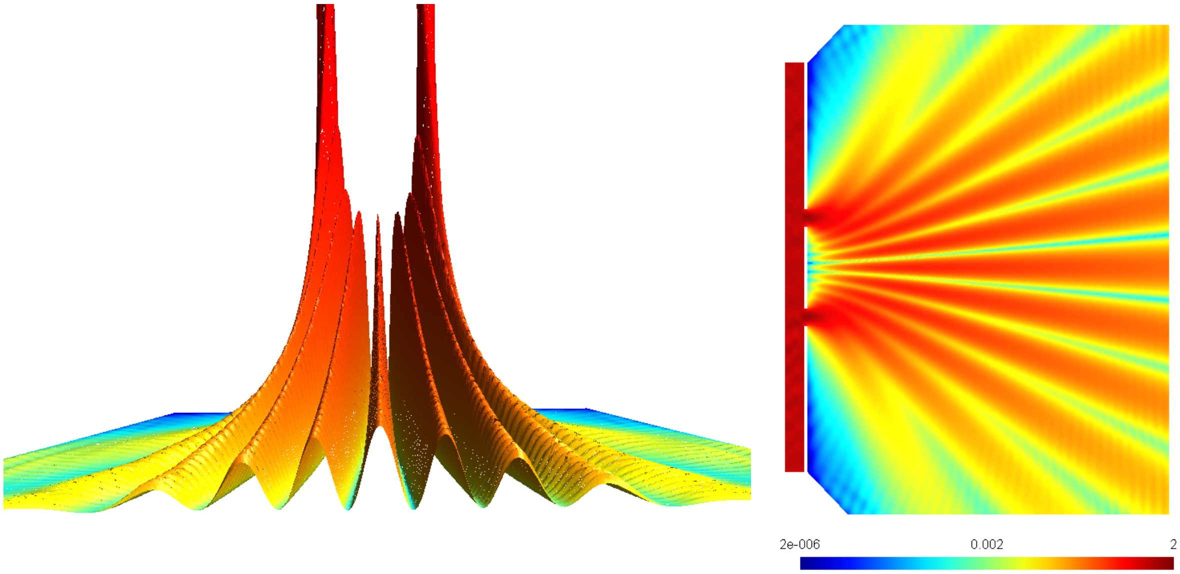

Figure 4.12: Time averaged intensity from modelling Young's experiment with a logarithmic colour scale. On the right, filled isolines of the solution. The left image has been rotated in space.

accomplished exactly through geometrical theories (in this application geometrical optics can bypass the restriction of only being applicable to high frequency waves). Therefore, the only assumption in this approach is the approximation that the EM waves emitted from the slits have spherical wavefronts. If this assumption is true, the m^{th} bright fringe must satisfy the following equations from the geometrical argument that the difference in distance from either slit to the bright fringe is given by $m\lambda$,

$$L^2 = (y + \frac{d}{2})^2 + R^2 \tag{4.6a}$$

$$(L + m\lambda)^2 = (y - \frac{d}{2})^2 + R^2. \tag{4.6b}$$

Here L is the length from one point source to the m^{th} local maxima situated at (R, y), and $L + m\lambda$ is the distance from the other point source to this maxima. As before, R is the distance from the aperture to the screen and d is the distance between point sources. L and y are unknowns to the system, which can be solved for the desired variable y as

$$y^2 = \frac{4m^2\lambda^2(d^2 + R^2) - m^4\lambda^4}{16d^2 - 4m^2\lambda^2}. \tag{4.7}$$

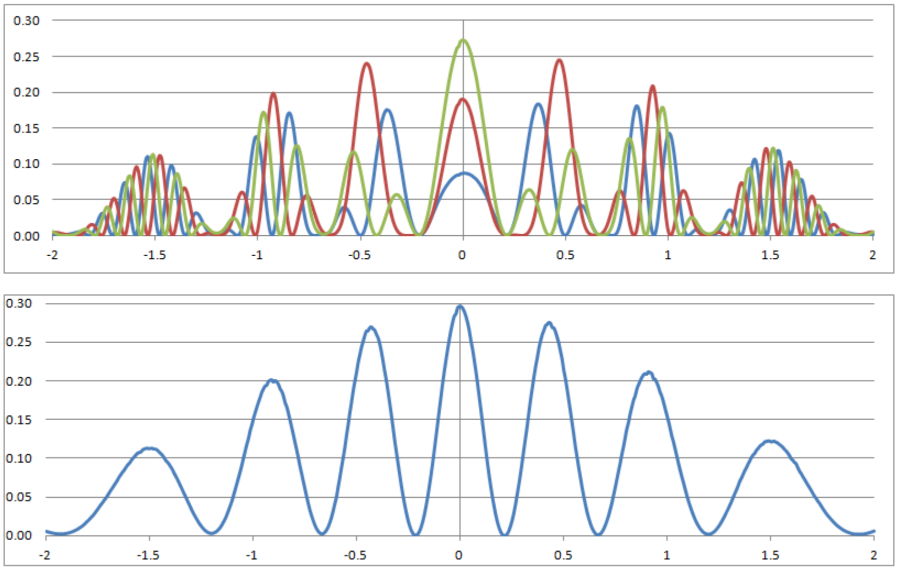

Figure 4.13: Intensity data from three instances in time (top), and the maximum of all sampled moments in time showing the amplitude of the oscillations in intensity along the line $x = 2.4$.

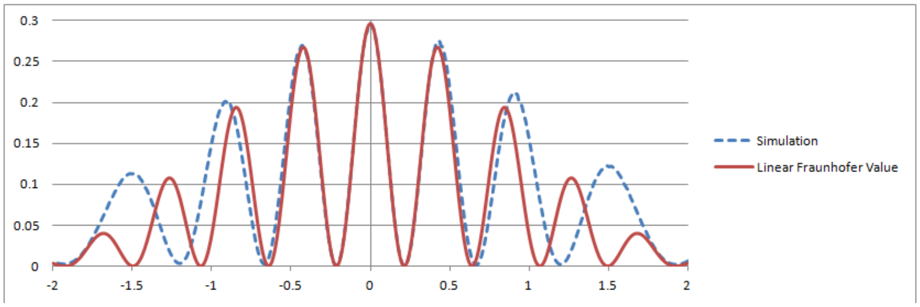

Figure 4.14: Simulation data compared to linear Fraunhofer solution.

This analysis reveals that the first three bright fringes after the central one should be at $y = 0.4337, 0.9125, 1.5103$ (and by symmetry the negative values as well). The DGM simulation records these maxima at $y = 0.4288, 0.9098, 1.5110$ verifying that the DGM results are accurate. Referring back to figures 4.15 and 4.14, we see that there is quite a bit of disagreement in the position of the third peak between DGM and Fraunhofer diffraction

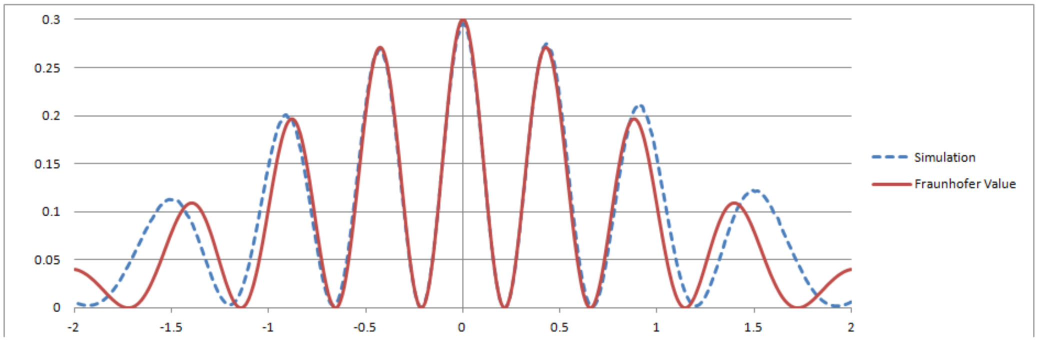

Figure 4.15: Simulation data compared to Fraunhofer solution.

theories. So this geometrical analysis confirms that the DGM method is in fact showing the correct distribution, whereas the Fraunhofer approximations are not particularly reliable in this range for this set of parameters.

4.3 Less Ideal Geometries - Parabolic and Hyperbolic Mirrors

One of the strengths of the DGM is its capability to handle complex geometries. Here we present two examples. Firstly, we model electromagnetic waves interacting with a parabolic mirror because this geometry has well understood behavior even in the presence of diffraction. Secondly, we combine a parabolic and a hyperbolic mirror. These geometries have applications within antenna design where the goal is to focus an electromagnetic signal from a distant source to a very small area.

The task of focusing a plane wave is done very near perfectly by a parabolic mirror (some loss occurs since the mirror is not infinitely long), however adding in the hyperbolic mirror is very useful in practical applications to allow the apparatus to work at a wider range of angles and to gain a lot more customization of where most of the intensity focuses.

A parabolic mirror's geometry is unique in the sense that it does not exhibit spherical aberration like the circular mirror. This means that all ray paths parallel to the axis of symmetry of the parabola will hit the mirror and reflect to the focal point with the same path length. This results in all rays from a plane wave reaching the focal point of the mirror at the same time and with the same phase. This results in the generation of a true focal point and is an example of a situation where geometrical ray optics predicts an intensity of infinity, a result which is of course never physically realized [36].

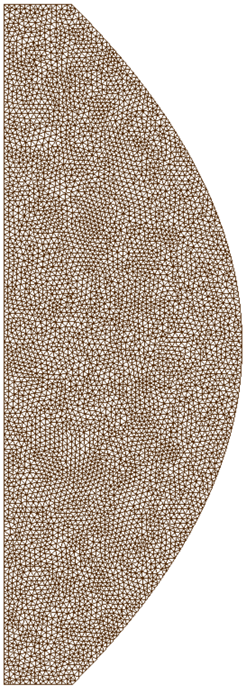

Figure 4.16: Mesh used to simulate the parabolic reflector

We begin with a simple parabolic mirror as shown in figure 4.16. A single planar wavefront is initialized by activating a forcing term in a narrow, vertical band of the domain prior to the mirror for half of one wavelength. This source term is given by

$$\vec{s}(x,y,t) = \begin{cases} (0,0,\sin(\frac{2\pi t}{0.03}))^T & \text{if } x \in (-0.1,-0.08) \text{ and } \frac{t}{0.03} \leq 0.5 \\ \vec{0} & \text{otherwise.} \end{cases} \tag{4.8}$$

We show a time lapse of the electric field at several instances in time in figure 4.17. Starting at the left, we observe a planar wavefront approaching the mirror. Upon interacting with the mirror, it produces a converging spherical wave, which focuses at a point before becoming a diverging spherical wave. The parabolic mirror is positioned such that the focal point should appear at $(0,0)$. Looking at either the time lapse images or the time averaged results, shown in figure 4.18, we see that the numerical solutions show a focal point located at $(0,0)$ with extreme accuracy.

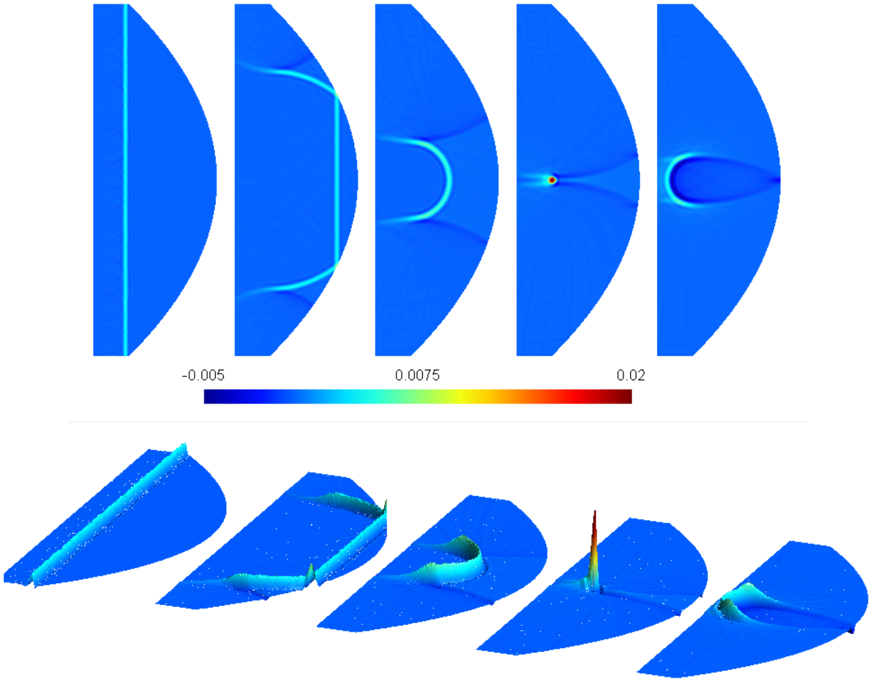

Figure 4.17: Electric field of a plane wave hitting a parabolic reflector at five different moments in time, progressing in time moving left to right.

Next we move on to the parabolic-hyperbolic pair. Here, we add the hyperbolic mirror inside the domain, this will block a minimal amount of the incoming wave, but it will redirect the focal point location closer to the surface of the parabolic mirror. This type of flexibility in the focal point position is of practical benefit for antenna construction [30]. These coupled reflectors are often called the classical Cassegrain reflector or antenna. In practice, antennas are often constructed using reflectors like this with a combination of lenses installed to allow even more customization [15, 16]. Systems involving parabolic and hyperbolic boundaries become challenging to model with methods relying on Cartesian grids such as FDTD. Furthermore, the flexibility in modelling and analyzing a single pulse or other broadband wave forms is advantageous when it comes to antenna optimization, and is not handled easily by frequency domain schemes such as MoM.

We simulate this problem on the mesh shown in figure 4.19 which has the hyperbolic mirror positioned to focus the pulse at $(0.5, 0)$. We apply the same forcing term as done in the previous simulation (4.8). In this numerical experiments it is difficult to analyze where

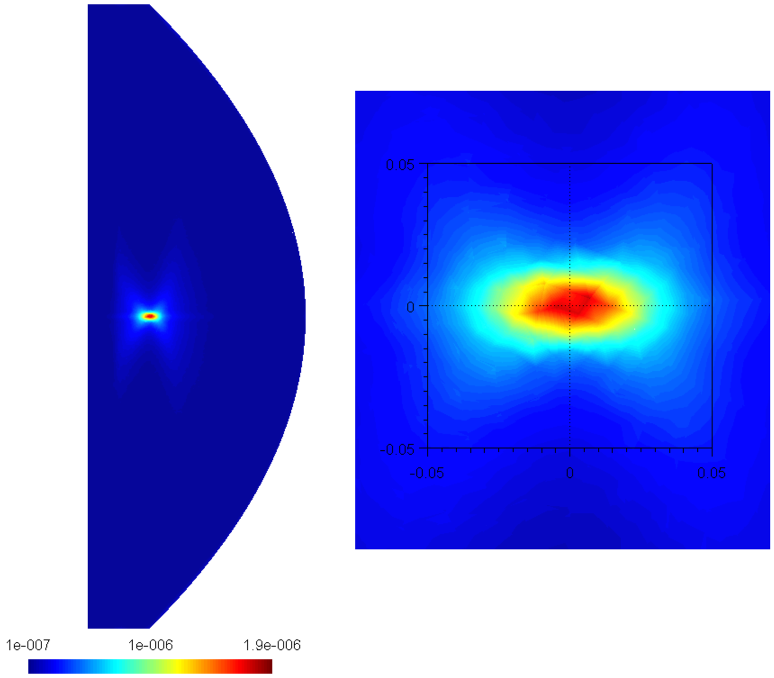

Figure 4.18: Time averaged intensity of the simulation of a parabolic reflector, on the right a zoom in of the focal region showing the high level of accuracy

the focal point appears since the hyperbolic mirror disrupts the nearly perfect converging spherical wavefront behavior seen in the parabolic mirror simulation. Adding in this extra element introduces more diffraction, which makes the solution harder to predict and control. In figure 4.20 we show the electric field distribution at six different time steps. We see that the planar wavefront diffracts around the corners of the hyperbolic mirror (figure 4.20, top-left). This effect and subsequent diffraction effects cause less of the intensity to converge to the theoretical focal point in comparison to the parabolic mirror simulation reported earlier. As a result, the location of the focal point becomes slightly shifted from the location predicted by GO, this is similar to what happened with the circular mirror. In the bottom centre image of this figure we see that when most of the wave is focusing, significant portions of the wave are elsewhere in the domain, illustrating that this geometry is much more complex to control and more valuable to model than the very simple parabolic mirror behavior. We also present the time averaged intensity in figure 4.21. Here, we see that focusing effects are certainly present, but the focal point is much more blurred than

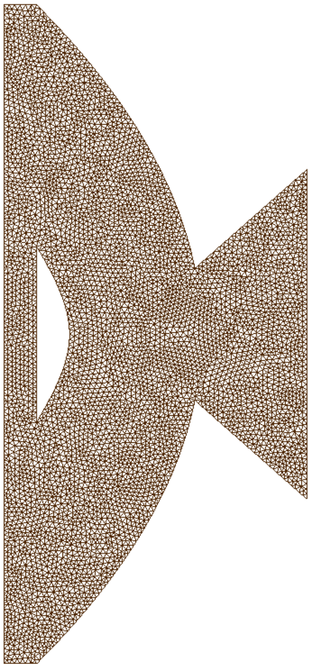

Figure 4.19: The mesh for simulations involving the parabolic-hyperbolic pair of reflectors.

it was before the introduction of the hyperbolic mirror. However, the numerical results demonstrate the two reflectors ability to focus the signal as desired and, again, we find that the DGM simulation has no difficulty in resolving the electromagnetic effects.

4.4 Refraction

Refraction is the property of electromagnetic waves or rays to change direction when entering a medium with a new refractive index. This phenomenon is the observable consequence of the fact that electromagnetic waves change speeds when entering a region of different refractive index. The geometry of refraction can be described using Snell's Law

$$\frac{\sin(\theta_1)}{\sin(\theta_2)} = \frac{n_2}{n_1} \tag{4.9}$$

where θ values are the angles between the velocity of the EM wave (or, equivalently, the direction of the ray) and the normal of the interface between the different media, as shown

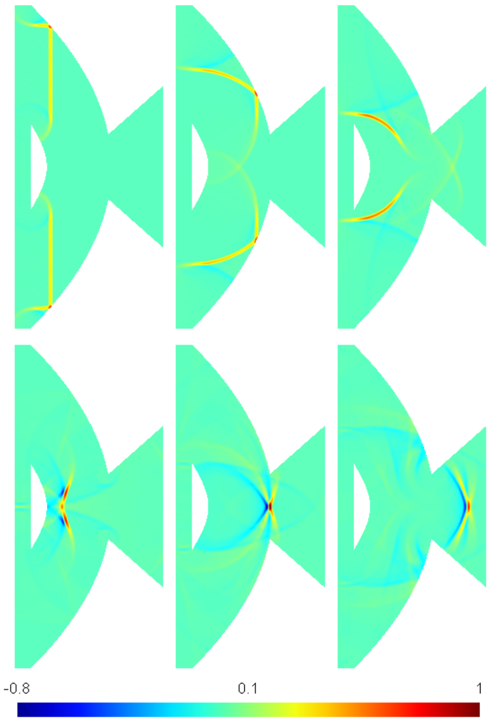

Figure 4.20: Images of the electric field at six different points in time as the pulse propagates through the domain.

in figure 4.22.

The refractive index of a medium is defined as

$$n = \sqrt{\frac{\epsilon}{\epsilon_o}\frac{\mu}{\mu_o}} \tag{4.10}$$

where ϵ_o and μ_o are the electromagnetic coefficients in vacuum, both scaled to be one for our simulations. It is worthwhile to note that the specific values of ϵ and μ are of little importance individually, since they become scaling factors on the electric and magnetic fields, but their product is very important as it defines the speed of propagation of the electromagnetic wave. As such, using $\epsilon = \mu = \sqrt{1.5}$ and $\epsilon = 1.5$, $\mu = 1$ will result in the same simulation up to scaling factors in the electric and magnetic fields.

To simulate refraction, we set up a 27320 element mesh to model the problem of a plane wave in one medium striking an interface at a 63.64 degree angle with a second

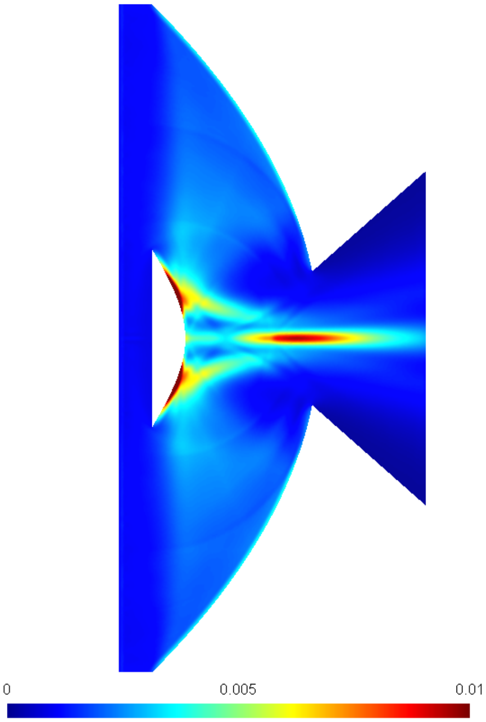

Figure 4.21: Time averaged intensity of the effects of a planar wave in a classical Cassegrain reflector.

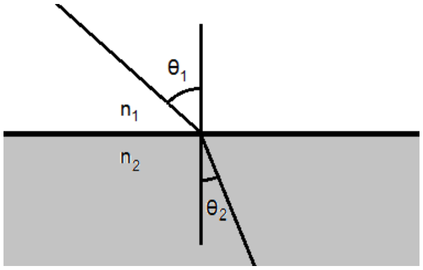

Figure 4.22: Snells Law for two media with indices of refraction of n_1 and n_2

medium behind it (see figure 4.23). We construct our mesh so cell edges are aligned along the interface between different media. This is beneficial since at the interface between two media, the electric and magnetic fields may become discontinuous. One can allow the

DGM to approximate discontinuous values within elements, however, it will be much more effective to place the static discontinuity in the solution along a static boundary where the value is assumed to be discontinuous and handled with the Riemann solver. We use indices of refraction of $n = 1$ ($\epsilon = \mu = 1$) and $n = 1.5$ ($\epsilon = \mu = \sqrt{1.5}$), typically used to represent air and glass, respectively. The outer boundaries on the long sides of the domain are set to be reflective (to allow plane wave propagation), and the other outer boundaries are set to be radiative to allow the waves to leave from these ends.

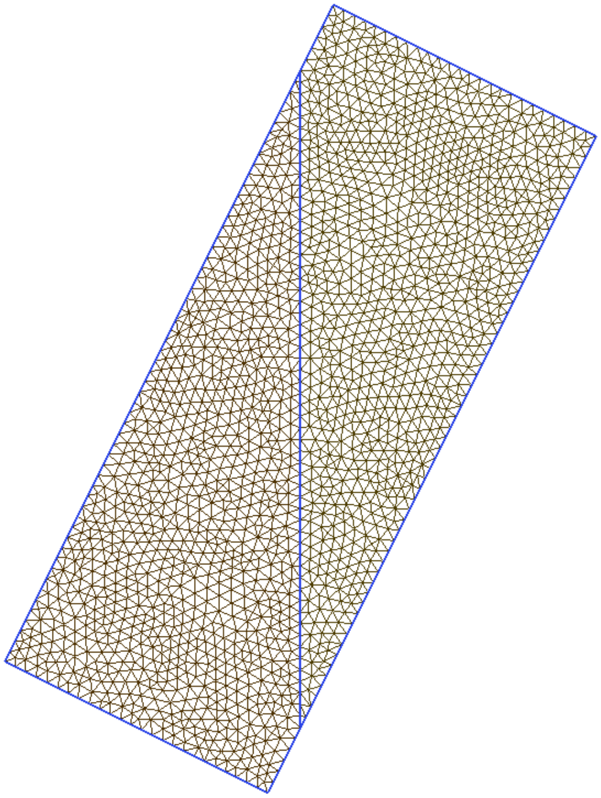

Figure 4.23: Mesh for modelling refraction between two media. The verticle line in the middle of the domain denotes the boundary between the different media.

We initiate an oscillating source which will create plane waves that will strike the interface at the 63.64 degree angle. The forcing term used to accomplish this is given by

$$\vec{s}(x,y,t) = \begin{cases} (0,0,\sin(\frac{2\pi t}{0.08}))^T & \text{if } (0.5x+y) \in (-1.12,-1.1) \\ \vec{0} & \text{otherwise.} \end{cases} \tag{4.11}$$

Although the effects of refraction are independent of wavelength for nondispersive media, we choose our source to make waves of length 0.08 (roughly 3.5% of the domain length) as this seems to be in the range which makes informative visualizations. According to Snell's law, we expect an angle of refraction of 36.68 degrees. In figure 4.24 (left), we demonstrate a ray path with the angle of incidence and expected angle of transmission. In figure 4.24 (right), we see the electric field at a specific time caused by a planar, oscillating source (at the bottom of the domain) striking the interface. We see the incident wavefronts approaching the interface perpendicular to the incident ray path as expected. The refracted wavefronts to the right of the boundary are also orthogonal to the predicted, refracted ray indicating the numerical solution agrees with the theory.

In figure 4.24 (right), we see two sets of reflections occurring. The first reflection occurs on the right-most outer boundary. The boundary condition here is set to be reflective in an effort to maintain plane waves, but the plane waves bend in the glass medium, causing them to no longer run parellel to this boundary so they reflect off of it. This was an expected consequence of the chosen boundary conditions. This reflection can be seen as the non-uniformity of the refractive waves in the lower portion of the glass medium. The second reflection is a similar effect occurring in the air medium which explains the non-uniform pattern along each wavefront in the top of the air medium. When EM waves strike an interface such as air-glass, some of the radiation is transmitted (and refracted), while some is reflected in what is known as a Fresnel reflection. So these reflections are also part of the correct solution for this simulation.

Fresnel reflections occur on nearly all interfaces between media and are governed by the Fresnel coefficients which determine how much of the energy is reflected and transmitted at a lossless interface. It is possible to create interfaces which feature no reflection (as is the goal of perfectly matched layer boundary conditions) and those which feature no transmission (which occurs in total internal reflection as discussed in the next section). Unfortunately, the Fresnel coefficients are relatively complex, which explains why perfectly matched layer boundary conditions for Maxwell's equations are not trivial to apply as demonstrated in [27, 4, 33].

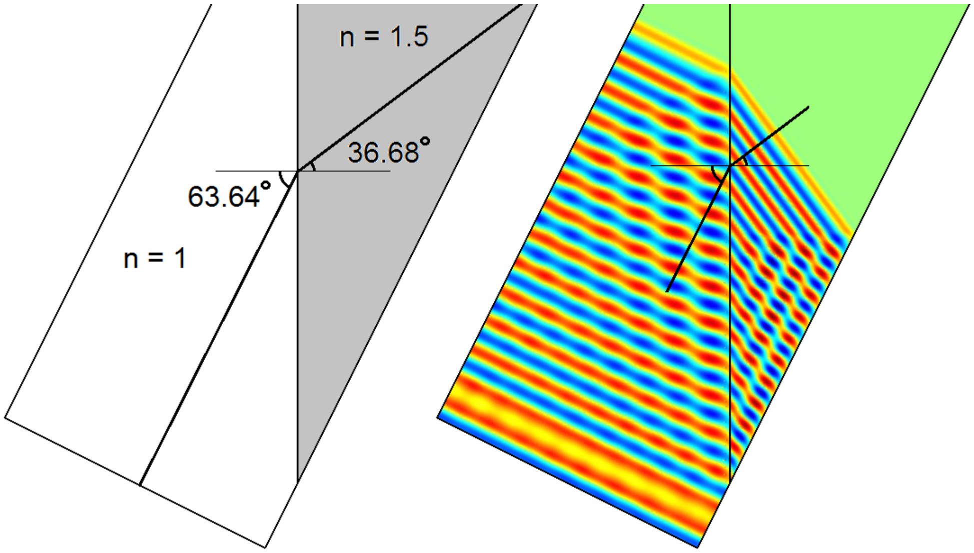

Figure 4.24: Refraction with angles. Left: a ray path for the solution with theoretical angles of incidence and reflection. Right: the simulated electric field at an instant of time compared to the theoretical ray showing good agreement.

4.5 Total Internal Reflection

If we repeat the simulation done in Section 4.4, but reverse the refractive indices of the media, so the source is in the $n = 1.5$ (glass) medium and beyond the interface $n = 1$ (air), the simulation should now feature total internal reflection. Total internal reflection occurs when electromagnetic waves strike an interface at an angle larger than the critical angle defined by

$$\theta_{critical} = \sin^{-1}(\frac{n_2}{n_1}). \tag{4.12}$$

This situation only occurs when the wave is travelling from a denser medium (with a larger index of refraction) into a less dense medium. The critical angle for glass to air is approximately 41.8 degrees. Since the angle of incidence is larger than this, the interface should act similar to a perfect mirror. To model this, we use the same set-up from section 4.4 with indices of refraction reversed. However, rather than using an oscillating source, we use a single wavelength as it will provide a more clear demonstration of the phenomena at play, most notably any changes in phase. At an intermediate time between when the wave is initialized and when it finally leaves the domain, we record the values of the electric field, and display it in figure 4.25. We see half of the planar wavefront which has not yet touched the interface, and the other half has been reflected off the interface, remaining in the glass medium on the left. A very close investigation reveals that some radiation manages to pass through the interface. Although this seems problematic, it is realistic at these scales. When the wave is reflected, the reflected wavefront immediately begins to diffract, and a small component of this diffracted wave is then eligible to pass through the boundary since its angle of incidence is close to zero degrees.

This simulation shows an incident wave described by one full wavelength of a sine wave, and a reflected wave which is also one full wavelength but now with a phase change. This is revealed by a careful look at figure 4.25 where we see the incident wave is described by a local maxima then a local minima, whereas the reflected waveform has a small local maximum in front, followed by a larger local minimum then another local maximum. An induced phase change is a feature of total internal reflection which depends on the angle of incidence. In this situation we see a very clear phase change, which is not quite a full 180 degrees. This simulation also features the usual diffraction effects whenever the plane wave is no longer being maintained by the reflective boundary condition.

4.6 Cylindrical Lens

Here we extend the simulation of refraction to a more complicated geometry. In this model we investigate the effects of placing a circular lens in the path of a Gaussian beam. In free space, Gaussian beams expand to form wider Gaussian beams as they propagate, a consequence of diffraction. However, lenses are able to change the beam's width profile, and even change a diverging beam into a converging one. A converging Gaussian beam will shrink in width until it reaches its minimum width, at which point it will begin diverging again.

We simulate a circular lens with radius 3.5mm located in the middle of a domain with dimensions 15mm by 15mm. Inside the lens, the medium is glass characterized by $\epsilon = 2.3$, $\mu = 1$, and outside is air with $\epsilon = 1$, $\mu = 1$. These lead to refractive indices of $n = \sqrt{2.3}$ and $n = 1$ respectively. We create a Gaussian beam centred vertically about $y = 0$ and originating 3.5mm before the lens and capture the electric field and intensity 3.5mm behind the lens as if it were striking a screen. The source term will create a Gaussian profile with beam waist of 0.35mm, or, equivalently, the intensity decays to e^{-1} of the max intensity at a vertical distance of 0.35mm from $y = 0$. We make the source oscillate to produce electric

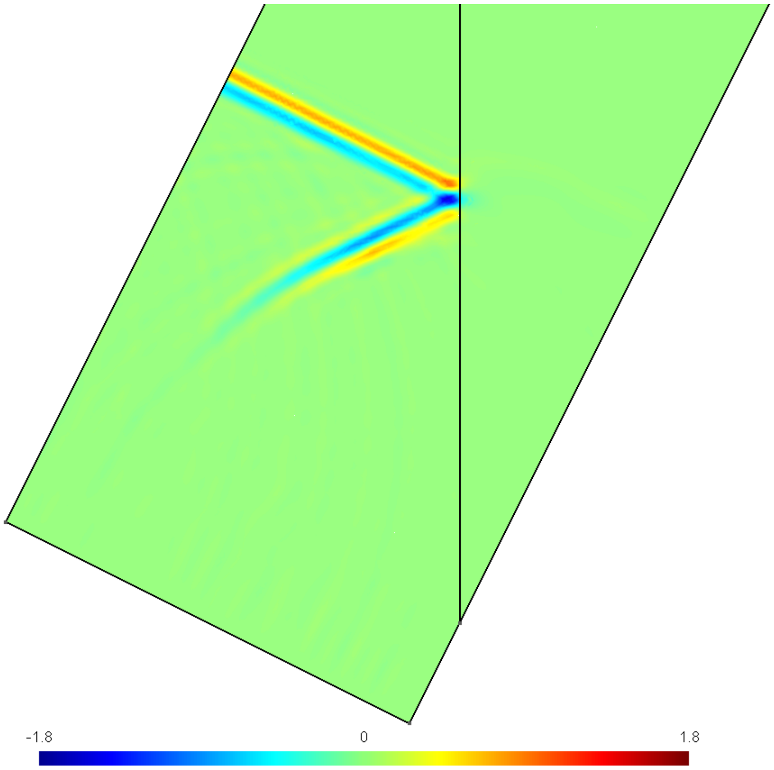

Figure 4.25: Total internal reflection at a glass (left) to air (right) interface of a single, planar wave

field waves with a wavelength of 0.35mm. The formula for this source term is

$$\vec{s}(x,y,t) = \begin{cases} (0,0,\exp(\frac{-y^2}{2(0.35)^2})\cos(\frac{2\pi t}{0.35}))^T & \text{if } x \in (-7.2,-7) \\ \vec{0} & \text{otherwise.} \end{cases} \tag{4.13}$$

We use a fourth order basis on each element, and use the 57079 element mesh shown in figure 4.26. Included in this figure are the first few wavefronts of intensity at an early time step before incidence with the lens. As previously done, we intentionally aim to put cell boundaries along the interface where the refractive index changes.

This experiment was simulated in [17] where they compared the results using the Transmission Line Matrix method (TLM) to FDTD and Spectral ray tracing (SRT) schemes. There simulations showed the diverging Gaussian beam striking the cylinder creating a

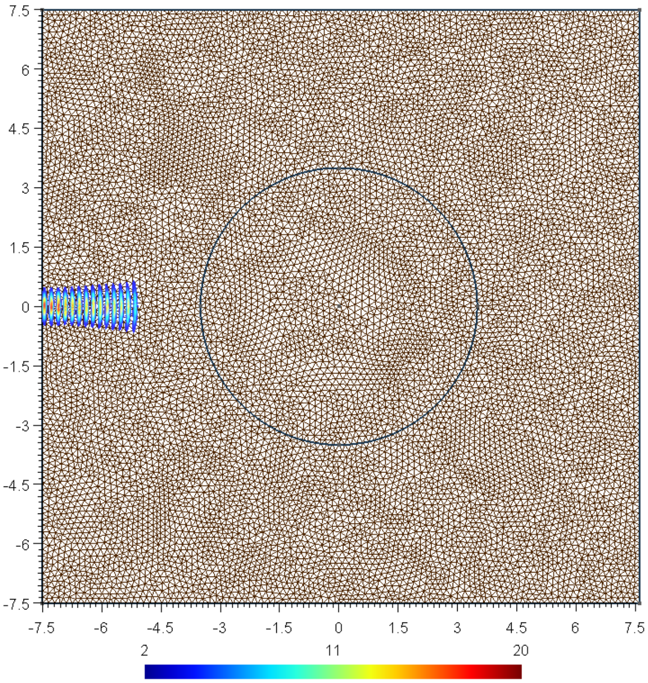

Figure 4.26: Mesh used for simulating a circular mirror and the first few waves of intensity from a Gaussian source.

planar wave with a vertical Gaussian profile within the lens, which then becomes a converging Gaussian beam upon leaving the lens. They also found visible reflections off both the glass-air and air-glass interfaces and calculated the amplitude of the electric field at the right boundary of the domain. They compare the amplitudes calculated by each of the three schemes at the vertical screen 3.5mm after the beam has left the circular lens (shown in figure 4.27, left).

Performing the simulation using the DGM results in similar results at the imaginary screen located at a distance 3.5mm behind the lens and throughout the rest of the domain. In figure 4.27 (right) we plot the maximum electric field amplitudes obtained on the simulated screen. The result shows closest agreement to the SRT and FDTD schemes. The peak value is slightly higher than the other techniques (all of which have been normalized to the original sources intensity), but, the Gaussian distributions width is very similar. Our implementation of the DGM for this problem applied simple, radiative boundary conditions along the edge of the domain which would be improved through the use of perfectly matched layer boundary conditions. A very careful inspection will show information reflecting off of these boundaries which accounts for the non-zero amplitude around ±4 in figure 4.27 (right), but these effects are extremely minor relative to the primary wave (approximately 1% of the amplitude of the primary wave).

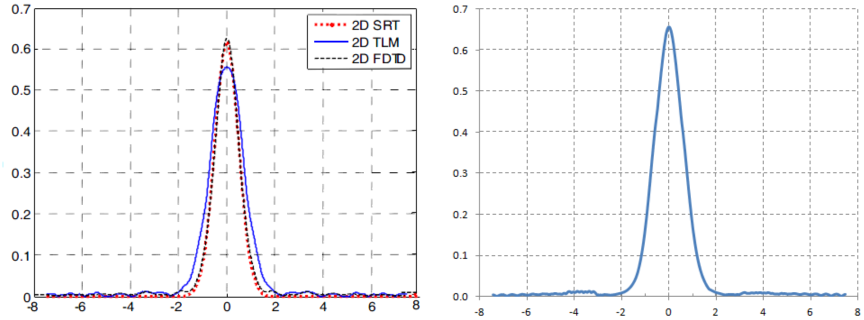

Figure 4.27: (left) A comparison of three schemes from [17], (right) the same simulation using DGM. The horizontal axis represents the height on the screen, and the vertical is the amplitude relative to the incident wave.

We also present the electric field in the domain in figure 4.28a which reveals a lot of the subtle effects such as the Fresnel reflections off the two interfaces the beam passes through. On the left of the lens is a well defined interference pattern also visible in the numerical solutions in [17], and inside the lens the reflections create a focal point effect. The pattern of the Gaussian beam changing from a diverging beam to a planar one, then to a converging Gaussian beam is visible in the DGM simulations and agrees with the other schemes in [17]. The time averaged intensity data also nicely illustrates the evolution of the Gaussian beam in figure 4.29. In the time averaged intensity data, we see some minor ripple effects caused by the reflections off of the boundaries of the lens. In this image we have set the maximum intensity rather low and saturated all values above this to make the visualization of the beam width as clear as possible.

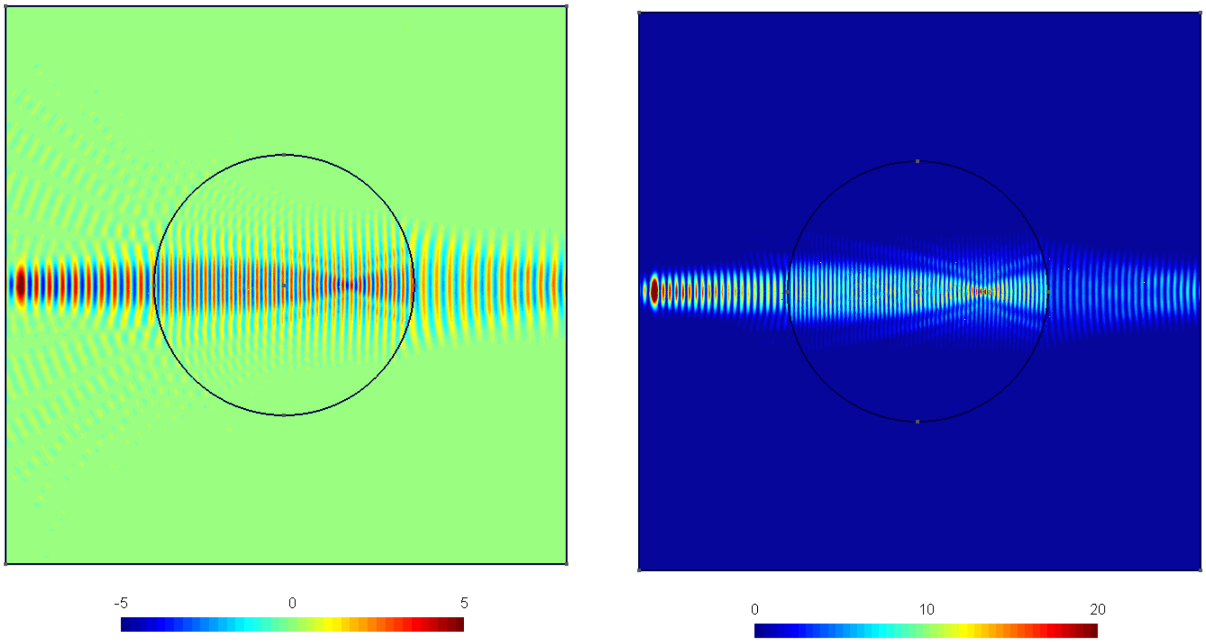

(a) Electric field (b) Intensity

Figure 4.28: Electric and intensity distributions at a fixed point in time of a Gaussian beam passing through a circular lens

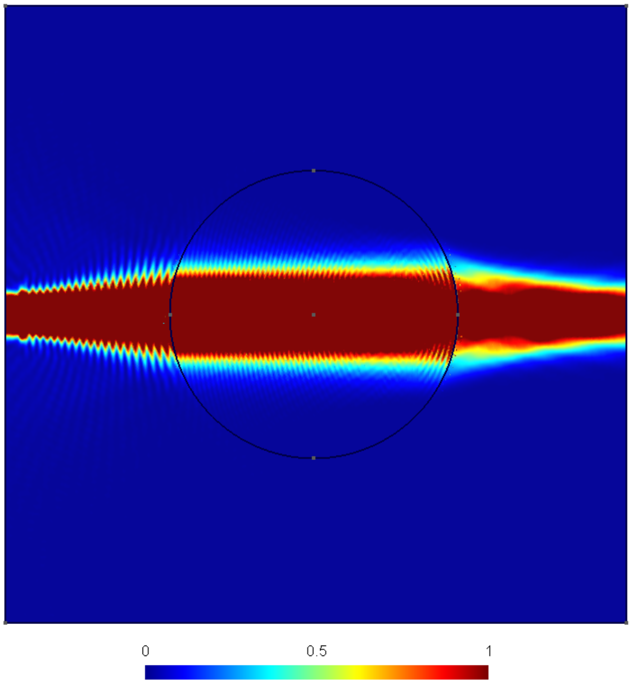

Figure 4.29: (Saturated) average intensity of a Gaussian beam passing through a circular lens

Chapter 5

Conclusion and Future Work

The range of problems within computational electromagnetics is very diverse. No numerical scheme can possibly be optimal for all of these applications. However, a highly robust scheme such as DGM may be very useful for many of these applications since its only limitation is its high computational cost. As computational power increases, this limitation will become less restrictive and the range of the DGM will expand to problems which are currently impractical to simulate.

We applied the DGM scheme to Maxwell's equations, which allows us to numerically approximate the macroscopic view of electromagnetics these equations represent. We demonstrated the ability to accurately model reflective boundaries as well as Fresnel reflections and transmission at the interface of two distinct media in the DGM framework. Combined with the use of perfectly matched layer boundaries to represent absorption, this shows that the DGM has the functionality to handle all of the different types of boundary properties featured in electromagnetic wave propagation. The DGM solutions to Maxwell's equations also properly demonstrate the effects of diffraction and interference as illustrated in Section 4.2.

Furthermore, since the DGM uses a unstructured grid, we are able to handle problems on complex geometries. We applied the DGM to circular, hyperbolic and parabolic mirrors as well as circular lenses, all of which rely heavily on a flexible mesh. Refinement can be performed on either the mesh size (h-refinement) or on the order of the basis functions on a given element (p-refinement). These are essential for time domain electromagnetics where the numerical solution needs to be able to accurately resolve the wavelengths in the problem. Having the flexibility to improve accuracy of the solution in two distinct ways offers a lot of customization to the scheme and can be used to gain increases in performance without requiring a longer run-time as was seen in Section 4.1. The DGM also has a local formulation which promises to offer a significant increase in the speed of computations through parallelization.

The DGM is also capable of handling solutions which include discontinuous or nearly discontinuous data. This is important when simulating applications which are susceptible to forming caustics or focal points which often occur from reflections. We simulated the caustic formed by a circular mirror (Section 4.1), and the focal point created from a parabolic mirror (Section 4.3), and found that in both scenarios the DGM offered an accurate and reliable approximation provided the element size was sufficient to capture the behavior. The DGM also accurately resolves the discontinuous values of electric and magnetic field which occur at the interface between two media without introducing unwanted oscillations into the approximation. This situation occurs in the simulations in Sections 4.4 and 4.6 where we modelled the transmission of an electromagnetic wave from air into glass. In both simulations the DGM accurately resolved the discontinuities without introducing significant error into the approximation.

In the future, the DGM method could be extended to remove most, or possibly all, of the restrictions we used to set up our formulation. Some of these steps have been performed here, allowing us to generalize the DGM to work with various source terms and media with different indices of refraction. Other extensions include a variety of changes to the properties of the electromagnetic coefficients to allow dispersive, anisotropic and nonlinear media. One could also implement lossy and conductive media to simulate applications outside of standard electromagnetic wave propagation. Most of these changes would cause the system of equations to become non-linear, which would lead to a more complex flux function and would require restructuring in some steps in the formulation (Section 3.2). Fortunately, the DGM is frequently applied to non-linear equations in fluid dynamics so these extensions are possible. This offers another advantage over many other schemes such as frequency domain schemes; for which there is no clear extension to the scheme for non-linear partial differential equations.

It would also be very interesting to apply the DGM to a problem involving a complex lens geometry, e.g. the optical components of a camera, or media involving continuously varying electromagnetic parameters, e.g. human tissue, since the current formulation is capable of handling these scenarios. However, without specific knowledge of one of these systems, designing one to create meaningful solutions would be very challenging.

References

[1] M. Abramowitz and I.A. Stegun, editors. *Handbook of Mathematical Functions.* Dover, New York, 1965.

[2] M. Ainsworth. Dispersive and dissipative behavior of high order discontinuous Galerkin finite element methods. *Journal of Computational Physics*, 198:106–130, 2004.

[3] H. Bagci, A.E. Yilmaz, A.C. Cangellaris, and E. Michielssen. Efficient broadband analysis of microwave components. *IEEE APS Symp. Digcst*, 2:170–173, 2002.

[4] J. Berenger. A perfectly matched layer for the absorption of electromagnetic waves. *Journal of Computational Physics*, 114:185–200, 1994.

[5] A. Bondeson, T. Rylander, and P. Ingelstrom. *Computational Electromagnetics.* Springer, 2005.

[6] A.C. Cangellaris and D.B. Wright. Analysis of the numerical error caused by the stair-stepped approximation of a conducting boundary in FDTD simulations of electromagnetic phenomena. *IEEE Transcations on Antennas and Propagation*, 39.

[7] C.G. Chen, P.T. Konkola, J.F., R.K. Heilmann, and M.L. Schattenburg. Analyses of vector Gaussian beam propagation and the validity of paraxial and spherical approximations. *Journal of the Optical Society of America A*, 2002.

[8] M.H. Cloudhury. *Electromagnetism.* Ellis Horwood Limited, 1989.

[9] B. Cockburn, S. Hou, and C. Shu. The Runge-Kutta local projection discontinuous Galerkin finite element method for conservation laws iv: The multidimensional case. *Mathematics of Computation*, 54:545–581, 1990.

[10] B. Cockburn, G.E. Karniadakis, and C. Shu. The development of discontinuous Galerkin methods. 1999.

[11] B. Cockburn and C. Shu. TVB Runge-Kutta local projection discontinuous Galerkin finite element method for conservation laws ii: General framework. *Mathematics of Computation*, 52:411–435, 1989.

[12] G. Cohen, X. Ferrieres, and S. Pernet. A spatial high-order hexahedral discontinuous Galerkin method to solve Maxwell's equations in time domain. *Journal of Computational Physics*, 216:340–363, 2006.

[13] D.A. Dunavant. High degree efficient symmetrical Gaussian quadrature rules for the triangle. *International Journal for Numerical Methods in Engineering*, 21(6):1129–1148, 1985.

[14] S.A. Galema. Microwave chemistry. *Chem. Soc. Rev.*, 26:–, 1997.

[15] D.M. Hailu, I.A. Ehtezazi, M. Neshat, G.S.A. Shaker, and S. Safavi-Naeini. Hybrid spectral domain ray tracing method for fast analysis of millimeter-wave and terahertz integrated antennas. *IEEE Transactions on Terahertz Science and Technology*, 1, 2011.

[16] D.M. Hailu, I.A. Ehtezazi, and S. Safavi-Naeini. Fast analysis of terahertz integrated lens antennas employing the spectral domain ray tracing method. *IEEE Transactions on Terahertz Science and Technology*, 8, 2009.

[17] D.M. Hailu, S. Shahir, A. Rohani, and S. Safavi-Naeini. Transmission line matrix method for two-dimensional modeling of terhertz Gaussian beam propagation. *PIERS 2011 in Suzhou Proceedings*, 2011.

[18] E. Hecht. *Optics 4th Edition*. Pearson Education, Inc., 2002.

[19] J.S. Hesthaven and T. Warburton. *Nodal Discontinuous Galerkin Methods - Algorithms, Analysis, and Applications*. Springer, 2008.

[20] R. Hiptmair. Finite elements in computational electromagnetism. *Acta Numerica*, pages 237–339, 2002.

[21] F.Q. Hu and H.L. Atkins. Eigensolution analysis of the discontinuous Galerkin method with nonuniform grids. *Journal of Computational Physics*, 182:516–545, 2002.

[22] U.S. Inan and R.A. Marshall. *Numerical Electromagnetics.* Cambridge University Press, 2011.

[23] J.B. Keller. Geometrical theory of diffraction. *Journal of the Optical Society of America*, 52, 1962.

[24] T. Koornwinder. Two-variable analogues of the classical orthogonal polynomials. In *Theory and applications of special functions*, pages 435–495. Academic Press, 1975.

[25] L. Krivodonova and M. Berger. High-order accurate implementation of solid wall boundary conditions in curved geometries. *Journal of Computational Physics*, 211:492512, 2006.

[26] L. Liu, Z. Han, and S. He. Novel surface plasmon waveguide for high integration. *Optics Society of America*, 2005.

[27] T. Lu, P. Zhang, and W. Cai. Discontinuous Galerkin methods for dispersive and lossy Maxwell's equations and PML boundary conditions. *Journal of Computational Physics*, 200:549–580, 2004.

[28] L.N. Medgyesi-Mitschang and D. Wang. Hybrid methods in computational electromagnetics: a review. *Computer Physics Communications*, 68:76–94, 1991.

[29] P. Monk. *Finite Element Methods for Maxwell's Equations.* Clarendon Press, 2003.

[30] R. Padman, J. Murphy, and R. Hills. Gaussian mode analysis of cassegrain antenna efficiency. *IEEE Transactions on Antennas and Propagation*, AP-35, 1987.

[31] M.J. Piket-May and A. Taflove. Electrodynamics of visible-light interactions with the vertebrate retinal rod. *Optics Letters*, 18, 1993.

[32] M.J. Piket-May, A. Taflove, W. Lin, D.S. Katz, V. Sathiaseelan, and B.B. Mittal. Initial results for automated computational modeling of patient-specific electromagnetic hyperthermia. *IEEE Transactions on Biomedical Engineering*, 39, 1992.

[33] Z.S. Sacks, D.M. Kingsland, R. Lee, and J. Lee. A perfectly matched anisoropic absorber for use as an absorbing boundary condition. *IEEE Transactions on Antennas and Propagation*, 43, 1995.

[34] M.N.O. Sadiku. *Numerical Techniques in Electromagnetics.* CRC Press Inc., 1992.

[35] R.C. Spencer and G. Hyde. Studies of the focal region of a spherical reflector: Geometric optics. *IEEE Transactions on Antennas and Propagation*, AP-16, 1968.

[36] J.J. Stamnes and H. Heier. Scalar and electromagnetic diffraction point-spread functions. *Applied Optics*, 37, 1998.

[37] D.C. Stinson. *Intermediate Mathematics of Electromagnetics.* Prentice-Hall, Inc., 1976.

[38] J.A. Stratton. *Electromagnetic Theory.* McGraw-Hill Book Company, Inc., 1941.

[39] B. Szegó. *Orthogonal Polynomials.* American Math. Soc. Colloquium Publications, vol.23, Providence, RI, 1967.

[40] A. Taflove. *Computational Electrodynamics The Finite-Difference Time-Domain Method.* John Wiley and Sons, 2007.

[41] P.Y. Ufimtsev. *Fundamentals of the Physical Theory of Diffraction.* John Wiley and Sons, 2007.

[42] K. Umashankar and A. Taflove. *Computational Electromagnetics.* Artech House, Inc., 1993.

[43] Y.Z. Umul. Modified theory of physical optics. *Optics Express*, 12.

[44] V. Vogelsang. On the strong unique continuation principle for inequalities of Maxwell type. *Mathematische Annalen*, 289:285–295, 2002.

[45] K.S. Yee. Numerical solution of initial boundary value problems involving Maxwell's equation in isotropic media. *IEEE Transcations on Antennas and Propagation*, 14.